RECORD
2022/13

PETROPHYSICAL EVALUATION OF THE PERMIAN AND ORDOVICIAN IN OLYMPIC 1, CANNING BASIN, WESTERN AUSTRALIA

J Cass, L Normore, L Dent and J Roche

Government of **Western Australia**
Department of **Mines, Industry Regulation and Safety**

Geological Survey of Western Australia

Government of **Western Australia**
Department of **Mines, Industry Regulation and Safety**

RECORD 2022/13

PETROPHYSICAL EVALUATION OF THE PERMIAN AND ORDOVICIAN IN OLYMPIC 1, CANNING BASIN, WESTERN AUSTRALIA

J Cass, L Normore, L Dent and J Roche*

* JLR and Associates, PO Box 7575, Cloisters Square, Perth WA 6850

PERTH 2022

Geological Survey of Western Australia

REFERENCE
The recommended reference for this publication is:
Cass, J, Normore, L, Dent, L and Roche, J 2022, Petrophysical evaluation of the Permian and Ordovician in Olympic 1, Canning Basin, Western Australia: Geological Survey of Western Australia, Record 2022/13, 23p.

ISBN 978-1-74168-980-8
ISSN 2204-4345

Grid references in this publication refer to the Geocentric Datum of Australia 1994 (GDA94). Locations mentioned in the text are referenced using Map Grid Australia (MGA) coordinates, Zones 51 and 52. All locations are quoted to at least the nearest 100 m.

Published 2022 by the Geological Survey of Western Australia
This Record is published in digital format (PDF) and is available online at <www.dmirs.wa.gov.au/GSWApublications>.

Further details of geoscience products are available from:
First Floor Counter
Department of Mines, Industry Regulation and Safety
100 Plain Street
EAST PERTH WESTERN AUSTRALIA 6004
Telephone: +61 8 9222 3459 Email: publications@dmirs.wa.gov.au
www.dmirs.wa.gov.au/GSWApublications

Cover image: Journey to the centre of the Kimberley (© 2010 PL Schubert)

Contents

Figures

Tables

Appendices

Petrophysical evaluation of the Permian and Ordovician in Olympic 1, Canning Basin, Western Australia

J Cass, L Normore, L Dent and J Roche*

Abstract

The Ordovician interval cored in Olympic 1 is one of the best-documented cored intervals of the Nambeet Formation in the Canning Basin. Consequently, the Geological Survey of Western Australia (GSWA) entered into a collaborative core analysis agreement with the EP473 Joint Venture to acquire a suite of core plugs for stratigraphic and petroleum system testing and CO_2 geosequestration evaluation.

This report presents an integrated interpretation of petrophysical and petrographic data acquired at Olympic 1, assessing reservoir quality in the Ordovician and the impact of acoustic properties on seismic prospecting at the Meda unconformity. Volume of clay, porosity and saturation have been calculated from wireline logs to assist in the petrophysical evaluation and for comparison with X-ray diffraction, routine and special core analysis measurements.

The Nambeet Formation has been subdivided into a lower Fly Flat Member and an upper Samphire Marsh Member. The Fly Flat Member contains good storage capacity but very poor flow capacity. Quartz overgrowths and carbonate precipitation fill intergranular porosity, isolating much of the macroporosity, in which flow is then further impeded by calcite-rich laminae present throughout the sandstone. Together these characteristics lead to the Fly Flat Member being deemed low permeability and therefore unsuitable for geosequestration. Special core analysis has confirmed the Samphire Marsh Member has excellent seal capacity as pore throats are consistently measured to be microporous in all lithologies. Micropores in detrital clays are the principal pore system, with sufficient microporosity in mudstones to expect connected porosity. Gas shows correlate positively with clay volume, demonstrating this connectivity. Mechanical properties of limestone and mudstone lithologies should be investigated if proposing the Samphire Marsh Member as a seal for geosequestration, due to their contrasting reservoir properties.

Porosity within the Willara Formation is generally microporous and isolated, with dolomitization at the top of the interval affecting porosity enhancement. Early calcite cements and later recrystallization and stabilization of these cements have destroyed most primary and secondary porosity. Rare bitumen fills intercrystal pores in cemented vugs. The late timing of hydrocarbon migration has precluded early porosity preservation, leading to poor hydrocarbon reservoir storage and flow potential.

A full suite of log data can easily differentiate Goldwyer Formation shale from Grant Group claystone; however, at seismic scale their acoustic properties are comparable. It is likely this contributed to the shallow prognosis of the Meda unconformity in this well, and it explains the unexpected erosion of the Goldwyer Formation. Without the Goldwyer Formation, the primary target for this exploration well lacked a seal.

KEYWORDS: bitumen, Canning Basin, Fly Flat Member, Grant Group, Nambeet Formation, Olympic 1, Ordovician, Permian, petrophysics, porosity, reservoir quality, Samphire Marsh Member, volume of clay, water saturation, Willara Formation

Well overview

Olympic 1 is a vertical petroleum exploration well drilled by Buru Energy (May–June 2015) approximately 56 km southeast of Broome within Exploration Permit 473 (EP473) in the onshore Canning Basin of Western Australia (Fig. 1) (Buru Energy Limited, 2015a). The well was drilled to test the large fault-bounded structural closure over the Middle Ordovician on the 'Western Thangoo High' within the Broome Platform with primary and secondary conventional oil targets in the Willara and Nambeet Formations, respectively. The nearest offset wells are Cyrene 1 and Hedonia 1, 22 km to the west, and Kanak 1 and Goldwyer 1, 28 km to the west-southwest (Buru Energy Limited, 2015a,b).

The total depth of the well was 1447.5 m measured depth (MD). The data acquisition program included wellsite gas detection, drilling parameters, ditch cuttings assessment, wireline logging and conventional coring prior to being plugged and abandoned as a dry hole. No velocity surveys, wireline formation pressure tests or drill stem tests were conducted (Buru Energy Limited, 2015a).

The operator's post-drill analyses have been limited to semblance processing to extract shear arrivals and improve the compressional data quality. Post-well interpretation of all data acquired by the operator is published in the well completion report (Buru Energy Limited, 2015b). The Geological Survey of Western Australia (GSWA) has produced a sedimentological core description and conducted a core sampling and analysis program including geochronology, biostratigraphy, inorganic geochemical analysis, organic chemistry, petrography and routine and special core analysis studies, resulting in the inaugural

* JLR and Associates, PO Box 7575, Cloisters Square, Perth WA 6850

GSWA Digital Core Atlas (Normore et al., 2017). The Olympic 1 cored interval represents one of the best-known examples for integrating precise geochronology with conodont biostratigraphy for the Lower Ordovician (Normore et al., 2018; Dent et al., 2021a) and has recently been nominated as a type section for the Samphire Marsh and Fly Flat Members of the Nambeet Formation (Dent et al., 2021b). Thermal maturity and source rock potential from Olympic 1 organic-rich mudstone intervals from the Nambeet Formation are assessed in Dent and Normore (2017) and Normore and Dent (2017).

Geological setting

The Canning Basin hosts up to 15 km of Ordovician–Cretaceous sedimentary fill laid down during four major depositional cycles or megasequences (Kennard et al., 1994; Fig. 2). The Olympic 1 well was drilled on the Broome Platform, a mid-basin northwest to southeast trending basin high. In this well, the oldest Lower Ordovician megasequence (Larapintine 2 of Kennard et al., 1994) is truncated by the Grant Group diamictites of the youngest megasequence (Gondwanan 1 of Kennard et al., 1994).

The Lower – Middle Ordovician Willara and Nambeet Formations, together with the recently defined Yapukarninjarra Formation (Normore et al., 2021), form the base of the first megasequence and the oldest known depositional units in the basin. Olympic 1 reached total depth in the Nambeet Formation (Appendix 1). The Yapukarninjarra Formation has only been intersected in Barnicarndy 1, in the southwest Canning Basin. The Willara and Nambeet Formations consist of predominantly shallow marine deposits and are commonly conformably overlain by Middle Ordovician sedimentary rocks of the Goldwyer and Nita Formations.

The Permo-Carboniferous Grant Group was deposited during the fourth, Late Carboniferous – Permian megasequence, the base of which is defined by the regional Meda unconformity. The Grant Group consists predominantly of fluvial sandstones, but glacial features and deposits are common (Backhouse and Mory, 2020).

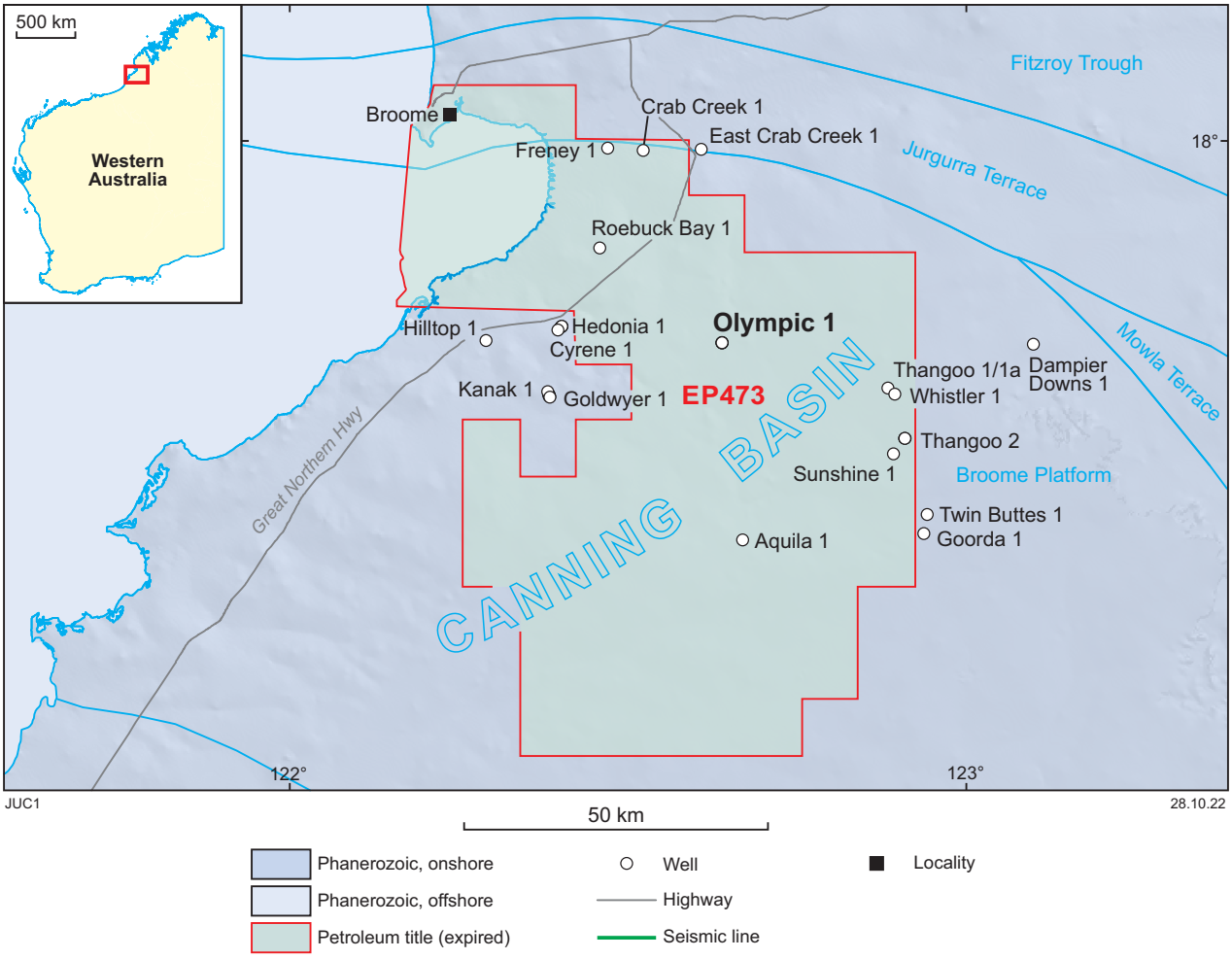

Figure 1. Tectonic subdivisions of part of the western Canning Basin showing the location of petroleum exploration well Olympic 1, other nearby wells within EP473, and the location of interpreted seismic data referenced in Figure 3

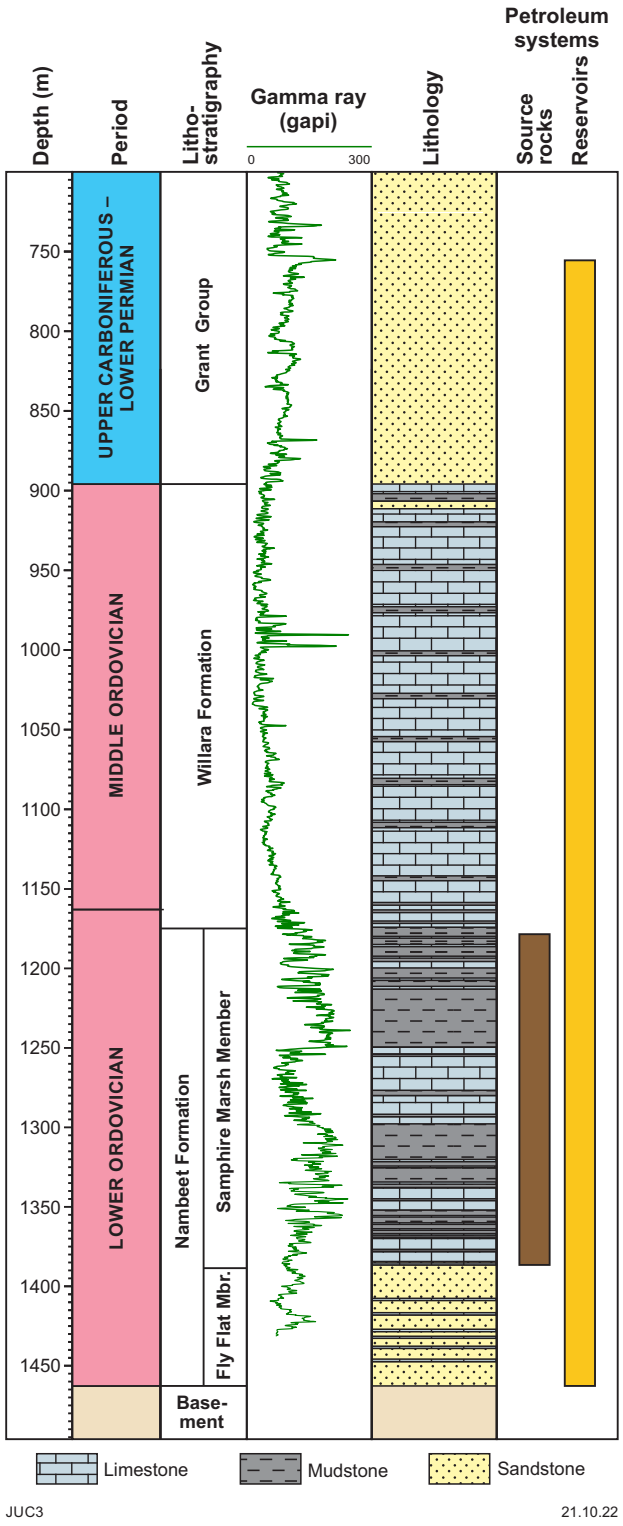

Figure 2. Permian to Ordovician stratigraphy of the Canning Basin showing generalized lithology and the position of potential source rock and reservoir intervals, and petroleum systems. Modified after Ghori (2013); time scale after International Commission on Stratigraphy (2013)

Formation evaluation

Data availability

Drilling and well data

A brief summary of the well construction and drilling fluids data used in this petrophysical interpretation is given in Table 1.

Mud logging data

Formation responses and drilling processes were monitored continuously. The formations encountered are all interpreted to be normally pressured with no movable hydrocarbons.

Cuttings were collected on a regular basis from surface to the top of the cored interval (Table 2). Minor oil shows were described from cuttings and core at the wellsite (Table 3). Automated gas detection was available via thermal conductivity for total gas detection and gas chromatography to detect individual hydrocarbon compounds, carbon dioxide and hydrogen sulfide. Minor gas shows were recorded at four depths, as significant departures from background gas levels (Table 4).

Wireline data

Weatherford Australia Wireline Services ran resistivity–density–neutron–sonic–gamma ray tools as single runs over the intermediate (156 mm [6.125″]) and total depth (96 mm [3.75″]) hole sections for formation evaluation and a cement bond log, through casing, over the top (216 mm [8.5″]) hole section to aid plug and abandonment activities, summarized in Table 5. All logs have been supplied with borehole and environmental corrections applied. Excellent logging conditions were encountered, except for minor borehole enlargement and rugosity between 750 and 875 m associated with the Grant Group. At the completion of drilling, the sonic waveforms have undergone semblance processing to extract shear arrivals and improve the compressional data quality.

Core data

The final 96 mm (3.75″) hole section of the well was continuously cored from 1128 to 1447.5 m in 6-m runs using wireline retrievable core barrels. Core recovery of 100% was achieved for the entire 319.5-m cored interval. This interval spans 272 m of the Nambeet Formation and the basal 47.5 m of the conformably overlying Willara Formation, representing an excellent reference section for the Nambeet Formation in the Canning Basin (Dent et al., 2021b). GSWA entered into a collaborative core analysis agreement with the EP473 Joint Venture to conduct a comprehensive analysis program including geochronology, biostratigraphy, inorganic geochemical analysis, organic chemistry, petrography and routine and special core analysis studies (Normore et al., 2017, 2018; Dent et al., 2021a,b).

Table 1. Well construction and drilling fluids summary

Hole section	*Interval (m MD)*	*Casing size*	*Shoe depth (m MD)*	*Mud type*	*Mud weight (ppg)*	*Max temp (°C)*
311 mm (12 ¼″)	3.4 – 29.1	244 mm (9 ⅝″)	29.1	Water	8.4 – 8.7	
216 mm (8 ½″)	29.1 – 698.0	178 mm (7″)	695.0	Gel polymer	8.5 – 9.0	
156 mm (6 ⅛″)	698.0 – 1125.0	127 mm (5″)	1122.9	KCl polymer	8.5 – 9.1	63
96 mm (3 ⅘ ″)	1125.0 – 1447.2	N/A	N/A	KCl polymer	8.5 – 9.1	80

Table 2. Rock sampling

Interval (m MD)	*Sampling frequency*
0 – 698	10 m composite cuttings
698 – 1125	5 m composite cuttings
1125 – 1447.5	6 m core lengths

Table 3. Oil shows recorded at the wellsite while drilling Olympic 1

Interval (m MD)	*Show description*
450 – 475	(Cuttings) Trace to sparse whitish yellow fluorescence in Arenaceous limestone. Slow whitish blue blooming cut. Thick to thin white residual ring. Very poor
875 – 880	(Cuttings) Trace (2–3%) Dull gold to goldish yellow fluorescence in limestone. No cut. No residual ring. Very poor
905 – 935	(Cuttings) 10% Whitish yellow fluorescence in limestone. No cut. No residual ring. Very poor
940 – 970	(Cuttings) 20% Dull greenish white fluorescence in limestone. Weak, slow bleeding to blooming, whitish blue. Weak to mottled whitish blue ring. Very poor to poor
1030 – 1035	(Cuttings) Trace – 10% whitish green – yellowish green fluorescence in limestone. Weak, slow white bleeding cut, moderate milky white crush cut. Weak, mottled whitish blue residual ring and film. Very poor
1128.5 – 1135	(Core) Very rare, weak oil bleeds assoc. with vugs, whitish green fluorescence in vuggy limestone. Very weak, slow, whitish blue bleeding cut. Weak, whitish blue, residual ring and film. Very poor
1362.1 – 1362.2	(Core) Moderate, whitish blue fluorescence in limestone. Weak, white streaming cut – weak white blooming crush crust. Weak, white, mottled residual film. Very poor
1393.5 – 1393.8	(Core) Moderate, whitish green fluorescence in sandstone, mottled white streaming cut grading to milky bloom. Weak yellow green residual ring. Weak white resin film. Poor

Table 4. Mud log gas shows recorded as significant departures from background gas levels

Depth (m MD)	*Background gas (units)*	*Peak gas (units)*	*Parts per million*						
			C1	*C2*	*C3*	*iC4*	*nC4*	*iC5*	*nC5*
1155	13.6	41	757.1	246	257	15.4	81.2	13	21.5
1165	13.3	40	538.6	218.9	254.4	28.6	110.3	19.6	33.7
1184	7.6	23.2	380.7	241.2	263.3	26.7	99.1	15.5	27
1201	8.2	24.5	442.7	400.2	674.4	85.6	309	57.2	84.1

Note: 1 unit = 0.02% or 200 ppm

Table 5. Olympic 1 wireline logging summary

Suite: run	*Logs*	*Interval (m MD)*	*Temp (°C)*	*Description*
1:1	MMR–MDL–MSS–MPD–MDN–MCG	1125 – 695	63	Compact Micro-Dual Laterolog–Sonic–Density–Neutron–Gamma ray
1:2	GR–CCL–CBL	695 – 10	63	Cement bond log
2:1	MFE–MDL–MSS–MPD–MDN–MCG	1447.2 –1123	80	Compact-Gamma ray–Resistivity–Density–Neutron–Sonic

GSWA compiled and published a Digital Core Atlas for this well that can be accessed via the Western Australian petroleum and geothermal information management system (WAPIMS) and the GSWA eBookshop (Normore et al., 2017). A complete set of all analyses is displayed with continuous gamma ray, compressional sonic and resistivity wireline log data and sedimentological interpretation products. Detailed results of the GSWA interpretation of the geochronology, biostratigraphy and geochemical samples are published (Dent and Normore, 2017; Normore and Dent, 2017; Normore et al., 2018; Zhen et al., 2020). Petrography, routine and special core analysis results form part of this petrophysical interpretation.

Petrography

A suite of 44 core samples were selected for petrographic analysis to determine the lithology, texture, mineralogy, diagenetic features and pore system of the cored interval. Thin sections were cut for each sample with subsets of plugs selected for regular scanning electron microscopy (SEM), argon ion milled scanning electron microscopy (AIM-SEM), cathodoluminescence microscopy (CL) and X-ray diffraction analysis (XRD) (Appendix 2). CL samples focused on carbonate lithologies while AIM-SEM were completed on mudstones (Normore et al., 2017).

Routine core analysis

Porosity, permeability and grain density measurements were attempted on 31 horizontal 25-mm (1″) diameter plugs. All plugs were cut with brine and cleaned of residual salts with warm methanol. Cleaned plugs were dried in a convection oven at 95 °C until plugs maintained a constant weight over a 24-hour period.

Grain volume was measured using the Ultrapore porosimeter. Pore volume and unsteady state permeability to air was measured using the CMS-300 at 800 psi confining stress. Together with length, diameter and weight measurements, porosity, permeability and grain density were calculated (Normore et al., 2017) (Fig. 3; Appendix 3). No measurements were made at overburden conditions.

Special core analysis

Mercury injection capillary pressure and flow studies measuring specific permeability to water and threshold pressure to CO_2 gas were conducted on three plugs to determine the seal capacity of the Samphire Marsh Member of the Nambeet Formation. All measurements were made at simulated overburden conditions. Measured properties are presented in Table 6 showing mercury injection entry pressure exceeded 10 000 psia, with no liquid permeability or CO_2 injection possible in the core plugs tested. These results confirm the tested lithologies could provide a potential seal for the underlying Fly Flat Member (Normore et al., 2017).

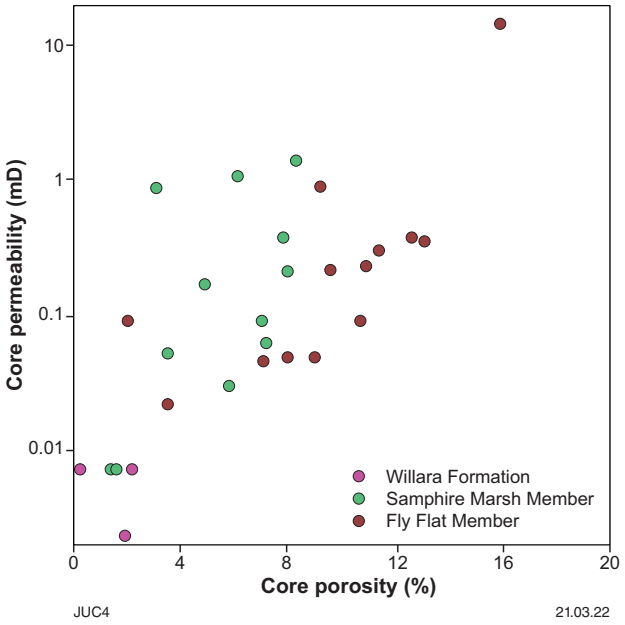

Figure 3. Core-measured permeability vs core-measured porosity coloured by formation

Petrophysical interpretation methodology

Interactive Petrophysics software (IP) was used to calculate volume of clay, porosity and water saturation. The environmentally corrected and merged log data suite and accompanying petrophysical interpretation is displayed in Figure 4. Data from routine core analysis porosity and XRD total clay volumes were used for wireline calibration. Oil and gas shows are also annotated on Figure 4.

Volume of clay

Volume of clay was calculated from gamma ray from 698 m to 1432 m. Resistivity, neutron and density–neutron volume of clay were also calculated from 898 to 1432 m, where the borehole conditions were excellent and all logs were good quality (Fig. 5). Parameters, annotated in Figure 5, were iteratively refined until the volume of clay was consistent across all calculation methods and validated by XRD total clay volumes (Fig. 6), giving an R^2 value of 0.87. The final volume of clay incorporates the variable grain density determined for porosity calculation.

Table 6. Summary of special core analysis results testing Samphire Marsh Member seal capacity and flow studies

Sample	*Depth*	*Hg injection entry pressure (psi)*	*Net confining stress (psi)*	*$Perm_{Brine}$ (mD)*	*CO_2 threshold entry pressure (psi)*
S3	1200.71	15226	1370	No flow	No injection
S1	1235.65	10355	1400	No flow	No injection
S2	1355.22	11774	1540	No flow	No injection

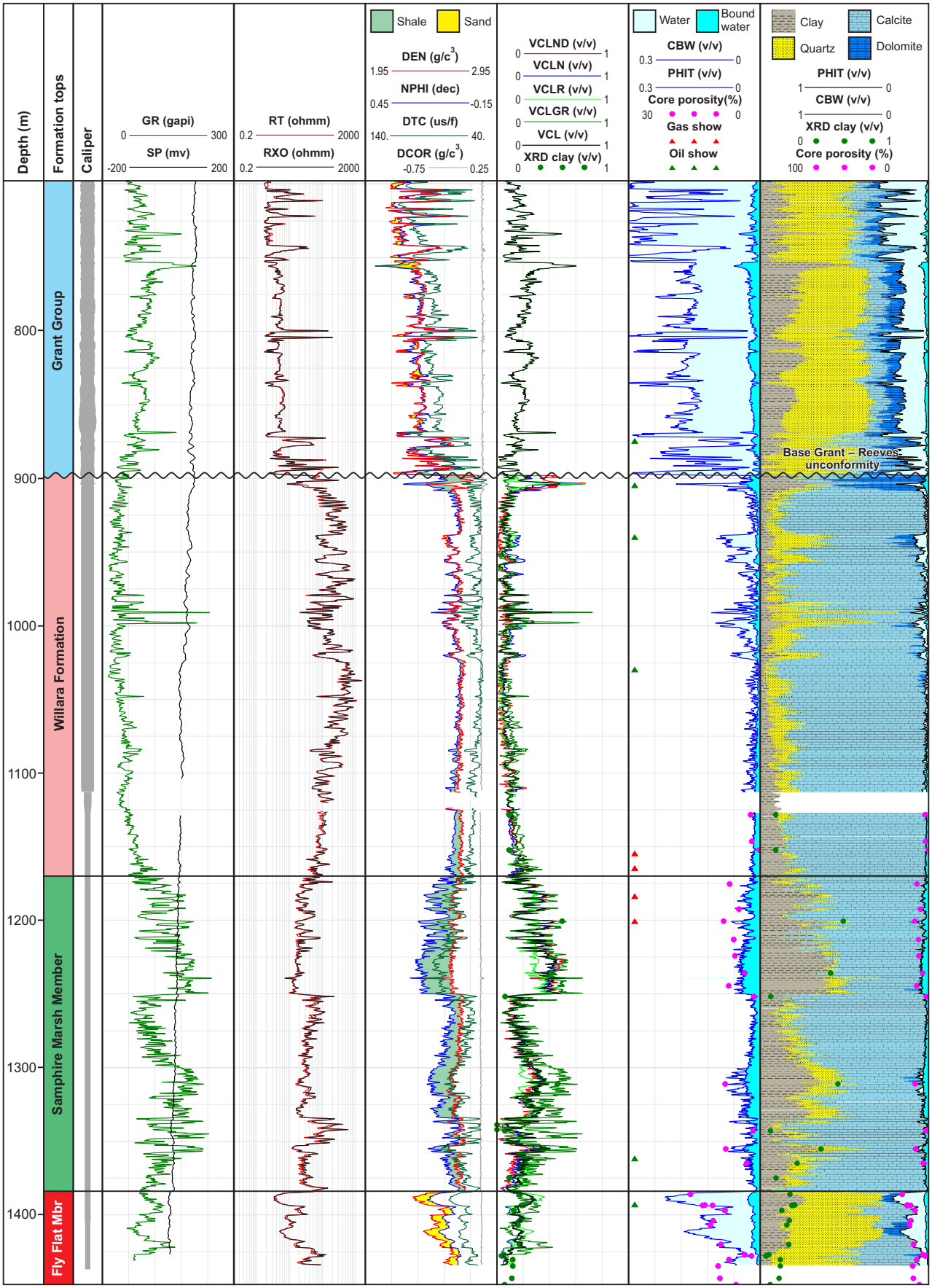

Notes: GR, gamma ray; SP, spontaneous potential; RT, true resistivity; RXO, invaded zone resistivity; DEN, density; NPHI, neutron; DTC, compressional sonic; DCOR, density correction; VCLND, volume of clay from neutron density; VCLN, volume of clay from neutron; VCLR, volume of clay from resistivity; VCLGR, volume of clay from gamma ray; VCL, volume of clay; XRD, X-ray diffraction; CBW, clay bound water; PHIT, total porosity

JUC5 17.11.22

Figure 4. Petrophysical interpretation summary for the Permian and Ordovician intervals of Olympic 1 with comprehensive wireline log coverage showing the hole conditions, wireline log coverage, interpreted volume of clay, total porosity, saturation and simplified quartz–limestone–dolomite–clay mineral model volumes with core measurements used for calibration and hydrocarbon shows documented at the wellsite

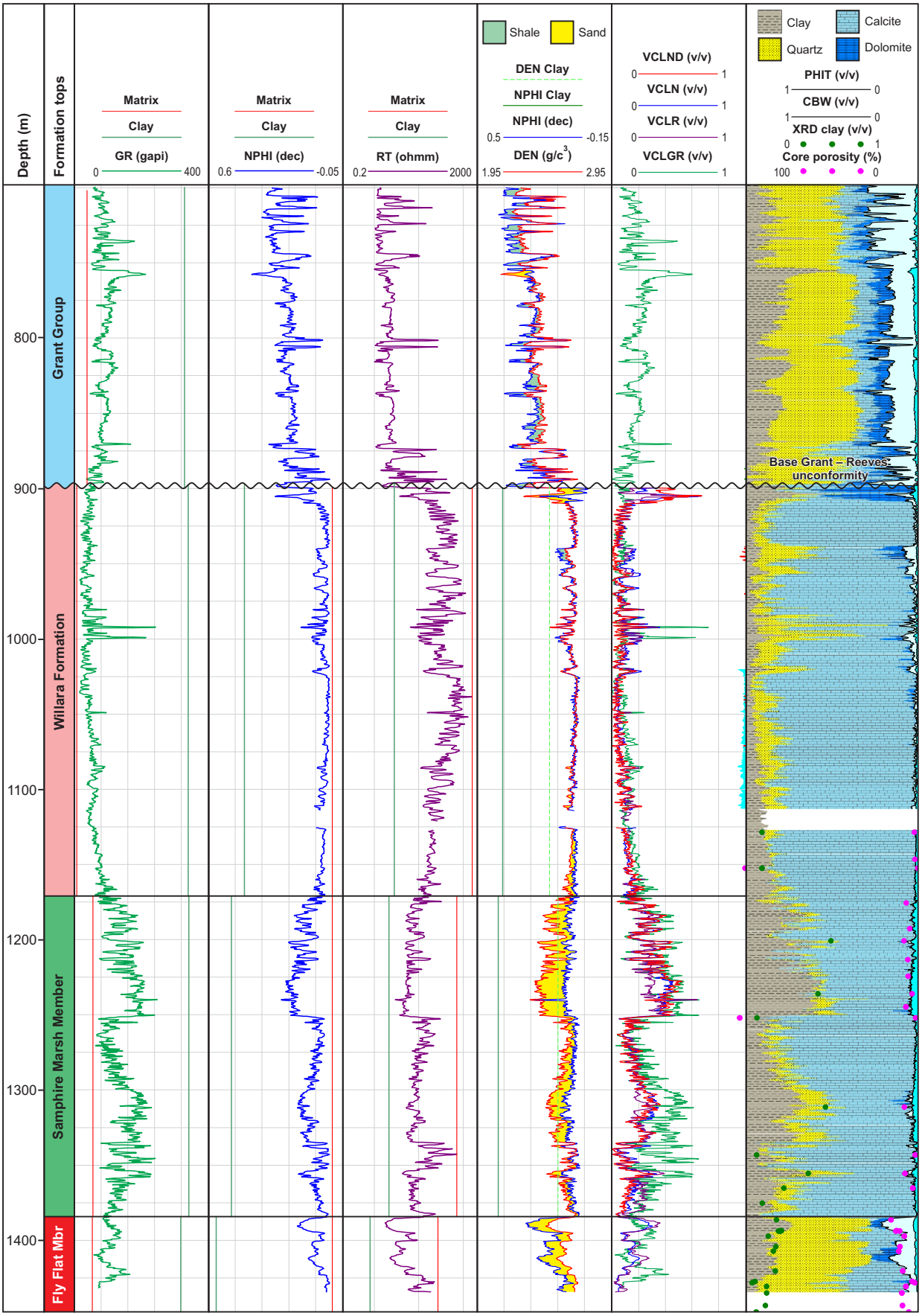

Notes: GR, gamma ray; NPHI, neutron; RT, true resistivity; DEN, density; VCLND, volume of clay from neutron density; VCLN, volume of clay from neutron; VCLR, volume of clay from resistivity; VCLGR, volume of clay from gamma ray

JUC6 21.10.22

Figure 5. Comparison of gamma ray, neutron, resistivity and density–neutron volume of clay calculation methods with matrix and shale points annotated, demonstrating convergence of each method in each interval

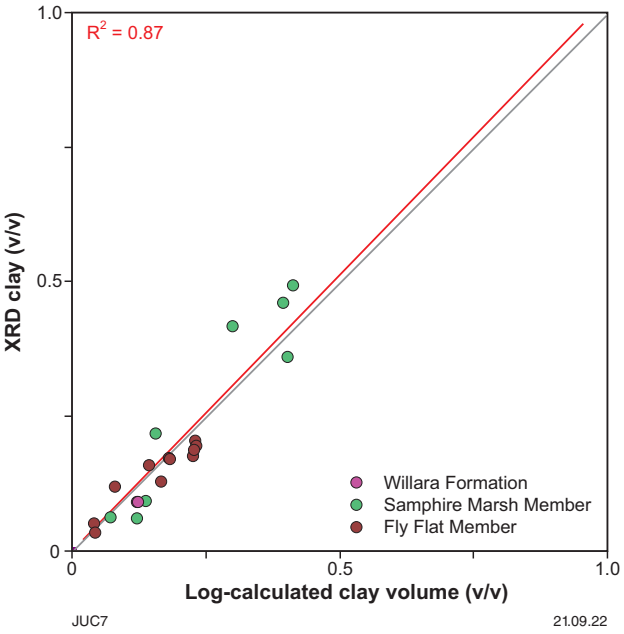

Figure 6. XRD-derived clay volume compared to final log-derived clay volume highlighting the excellent positive correlation achieved with an R^2 value of 0.87

Porosity

The final porosity curve was calculated from the density log. Density porosity was parameterized by initially solving a mineral model comprised of sandstone, calcite, dolomite and clay using density, sonic and photoelectric effect logs. Sandstone and calcite mineral volumes are well resolved by the log data and compare well with XRD analysis (Fig. 7a,b). Dolomite is less well resolved and compares poorly with XRD analysis (Fig. 7c). The density log was then hydrocarbon corrected and clay corrected before calculating grain density and porosity. Total log porosity is crossplotted against measured core porosity in Figure 8. Differences between log porosity estimates and core plug measurements are minor, resulting in an R^2 value of 0.81.

Saturation

Total water saturation was calculated using the Archie equation (Archie, 1952). A single water resistivity was estimated from the Pickett Plot (Pickett, 1973; Fig. 9) of 0.25 ohmm at 25 °C equivalent to salinity of 23 200 ppm NaCl. The saturation exponent, ***n***, was kept constant at 2 and a variable ***m*** exponent was calculated from the Shell formula (Equation 1) (Winsauer and Shearin, 1952). This caused ***m*** to change rapidly at low porosities, between 2.8 for effective porosities less than 2% and 2 for effective porosities equal to 10% through to 1.94 for effective porosities greater than 25%. Generally this results in ***m*** greater than 2 in carbonate lithologies and ***m*** between 1.94 and 2.1 in clastic lithologies in this well. All intervals are interpreted to be water filled.

$$m = 1.87 + \frac{0.018}{\emptyset_e} \qquad \text{(Equation 1)}$$

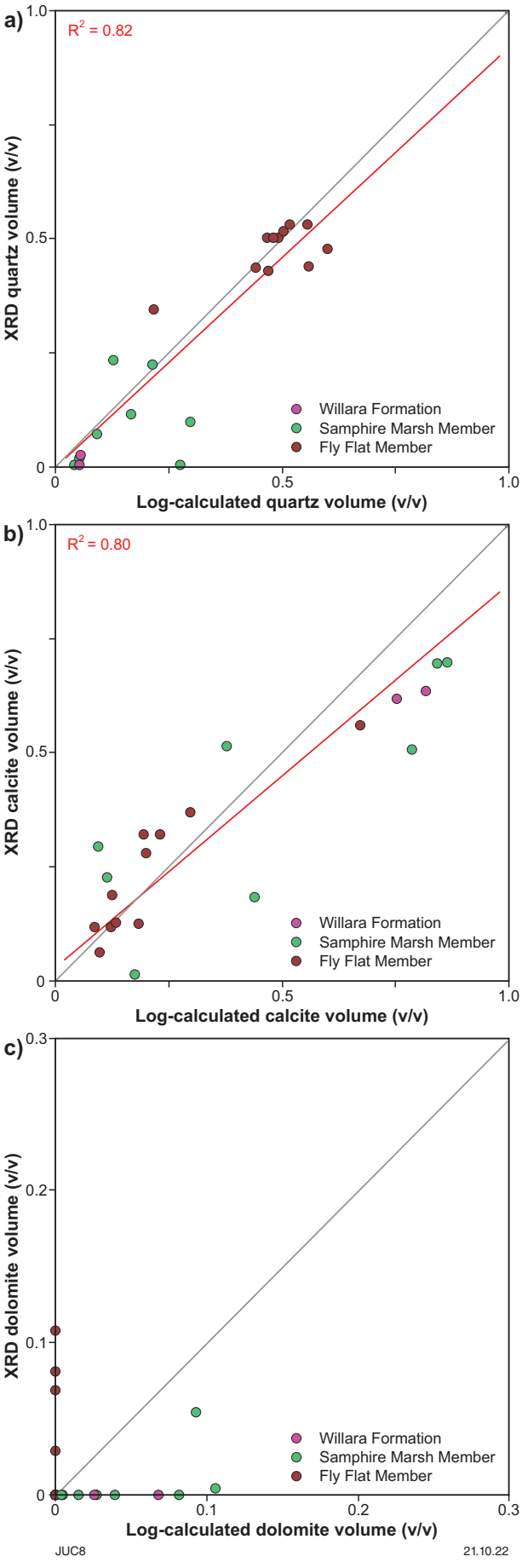

Figure 7. Comparison of XRD and log-derived mineral volumes: a) XRD quartz volume compared to log-estimated quartz volume; b) XRD calcite volume compared to log-estimated calcite volume; c) XRD dolomite volume compared to log-estimated dolomite volume

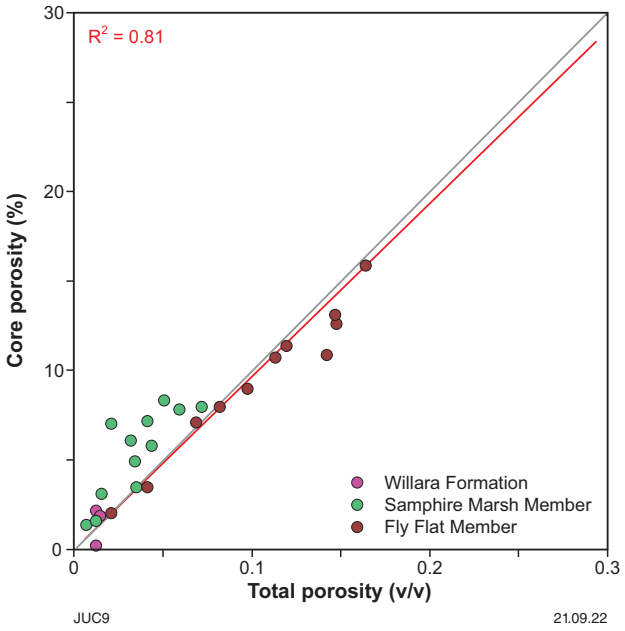

Figure 8. Core-measured porosity compared to log-derived total porosity highlighting the excellent positive correlation achieved with an R^2 value of 0.81

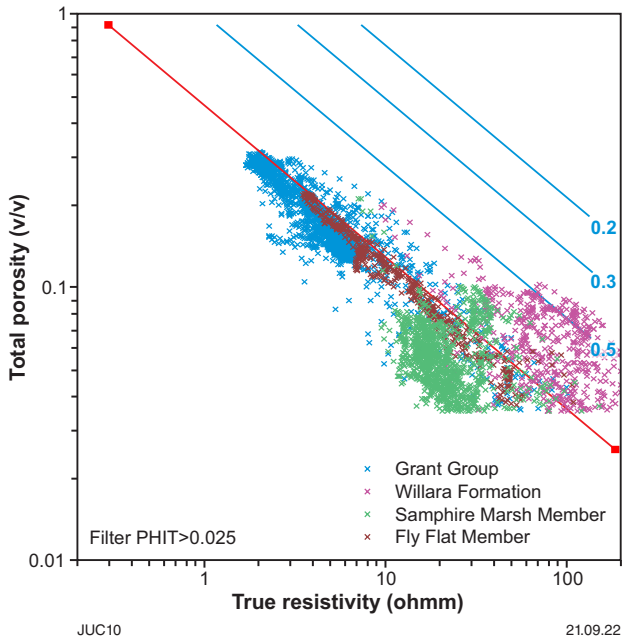

Figure 9. Pickett plot showing total porosity as a function of resistivity with water saturation annotations for water resistivity equivalent to 0.25 ohmm at 25 ℃ and *m* and *n* set to 2. The variable *m* calculation implemented in this evaluation has the effect of flattening the gradient of the saturation lines annotated on this plot for all porosity points less than 10% and gently increasing the gradient for all points greater than 10% porosity, resulting in very little scatter around 100% water saturation and all formations being interpreted as close to 100% water filled

Discussion

Nambeet Formation (1175.2 – 447.5 m)

The Nambeet Formation is fully cored to 1447.5 m with wireline log interpretation possible to 1432 m. It is divided into two formal members: the lower Fly Flat Member and the overlying Samphire Marsh Member, as described by Dent et al. (2021b). The Fly Flat Member is sandstone dominated and the Samphire Marsh Member is dominated by mudstone and carbonate lithologies.

Fly Flat Member (1383.3 – 1447.5 m)

The Fly Flat Member consists of medium to very fine-grained well-sorted subarkosic sandstone that is typically bioturbated with carbonate nodules common towards the top of coarsening upward sequences. The mineralogy of this unit is represented in a ternary diagram derived from XRD mineral analysis in Figure 10. Appendix 4 compares representative 50-cm core images, corresponding petrographic studies, and the core-measured porosity and permeability, characterizing the typical lithologies in this unit.

Core calibrated volume of clay is generally less than 20%, averaging 16% across the logged interval. Carbonate nodules, calcitic matrix and occasional fossil fragments and peloids contribute to the XRD volume of calcite, giving a broad range from 0 to 63%. Quartz volumes range from 30 to 60%, averaging 48% through the logged interval.

Routine core analysis of 14 samples provided a range of 2 to 15.9% porosity throughout the Fly Flat Member. Calibrated wireline interpretation of the medium-grained laminated sandstone at the very top of the Fly Flat Member host the best porosity, reaching 22% and averaging 17%, while the fine to very fine-grained interval averages 9.5% total porosity.

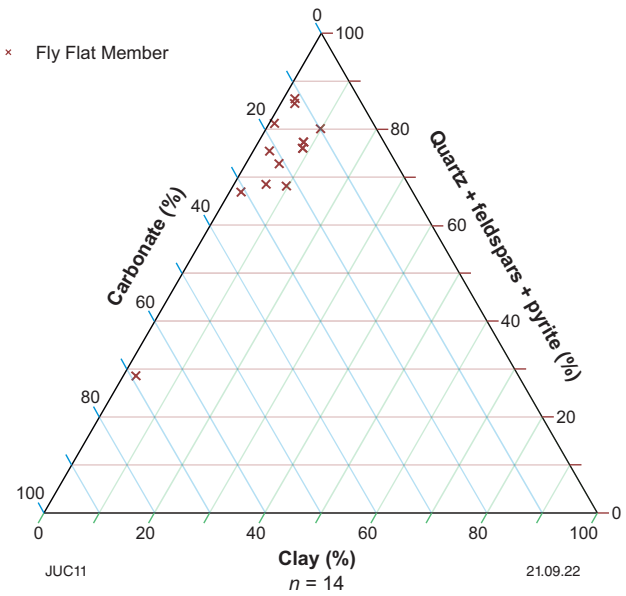

Figure 10. Ternary diagram characterizing the Fly Flat Member mineralogy from XRD analysis

Neutron-density data (Fig. 11) show porosity decreasing as data points trend away from sandstone lithology towards the limestone lithology. Thin sections reveal that carbonate is commonly present in thin layers through this interval (Fig. 12). The carbonate layers have no macro porosity, with the neutron-density porosity trend showing that as these layers become more abundant, matrix density trends away from sandstone density (2.65 g/cc) towards limestone density (2.71 g/cc) and overall porosity decreases towards zero. Post-depositional formation of dolomite and quartz overgrowths have destroyed primary porosity by filling intergranular pore spaces (Fig. 13). Conversely, porosity is created by post-depositional K-feldspar dissolution; plotting K-feldspar from XRD analysis against total porosity demonstrates a strong positive correlation, with an R^2 value of 0.88 (Fig. 14). The volume of clay within the sandstone portion of the matrix is relatively constant. Clay porosity is well preserved, consistently contributing 1–2% to total porosity.

A single oil show was recorded through this interval, with wireline interpretation confirming the interval is close to 100% water filled.

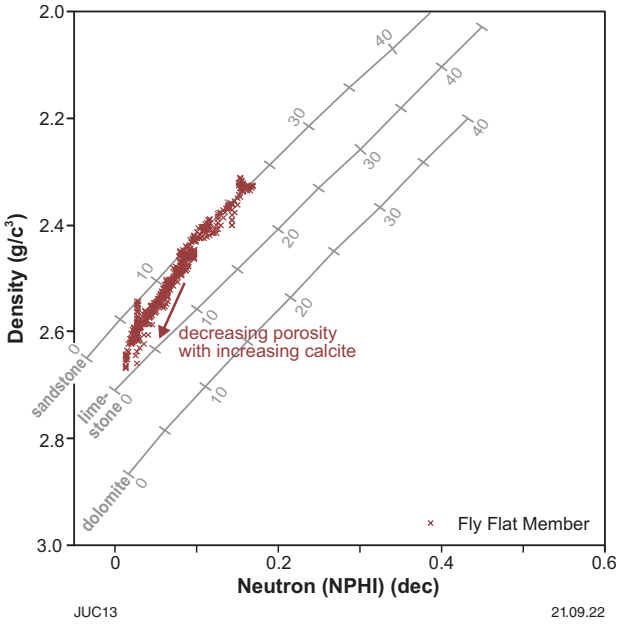

Figure 11. Neutron-density crossplot (Weatherford, 2007) showing the mineralogical controls on reservoir quality in the Fly Flat Member intersected at Olympic 1. This crossplot shows a sharp reduction in porosity as the abundance of carbonate laminae increase

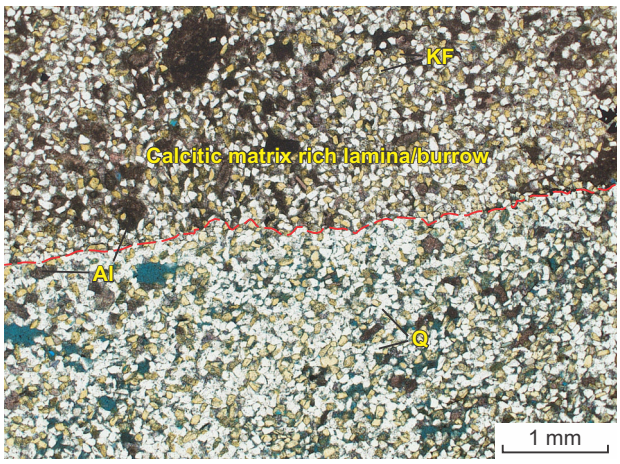

Figure 12. Thin section showing carbonate laminae common in the Fly Flat Member

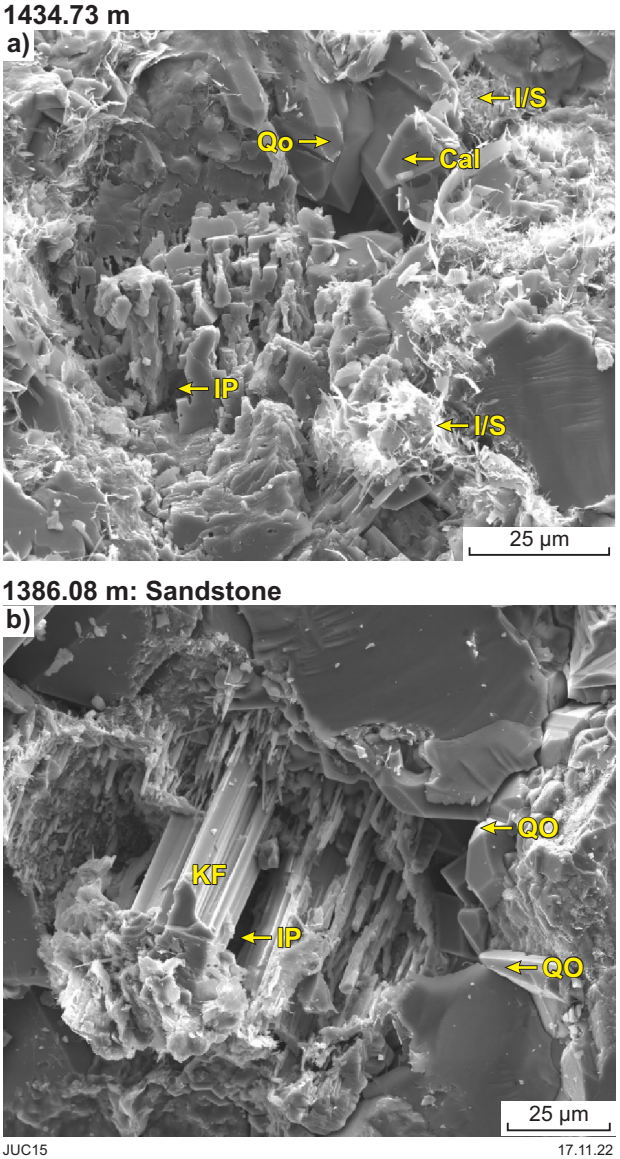

Figure 13. SEM photomicrographs showing: a) secondary porosity creation via K-feldspar dissolution and destruction of primary porosity by quartz overgrowths and calcite cements; b) secondary porosity creation via K-feldspar dissolution and destruction of primary porosity by quartz overgrowths filling intergranular porosity

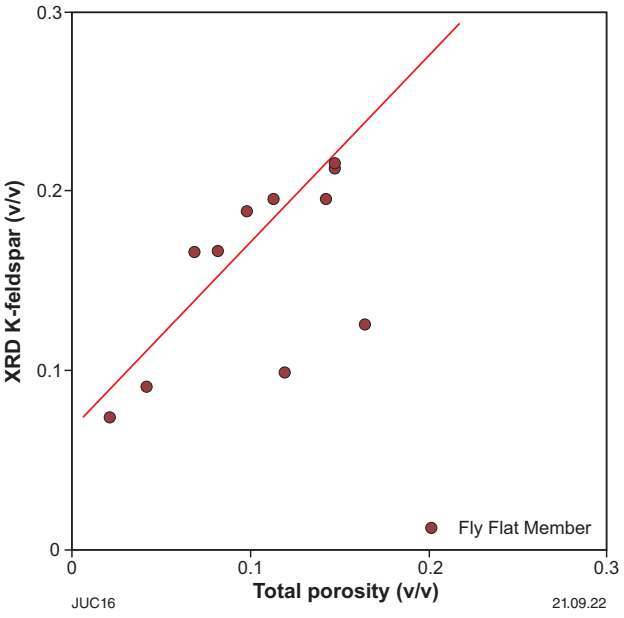

Figure 14. XRD K-feldspar volume vs total porosity showing porosity creation via K-feldspar dissolution

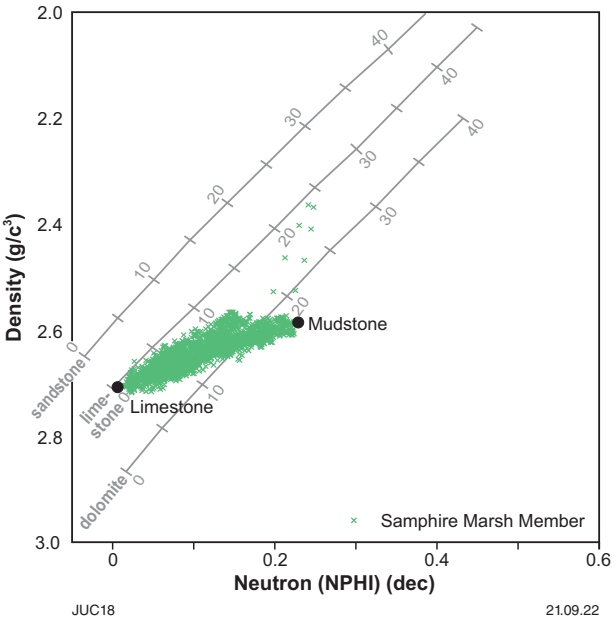

Figure 15. Neutron-density crossplot (Weatherford, 2007) of the Samphire Marsh Member with 100% limestone and 100% mudstone endpoints annotated, showing porosity increasing as the volume of limestone decreases and the volume of clay increases

Even though the average porosity of the Fly Flat Member indicates relatively good storage capacity, corresponding core-measured permeability is generally less than 0.1 mD, ranging from 0.0002 to 13.4 mD. The fine to very fine-grained character of the rocks, together with quartz overgrowths and calcite filling intergranular pore space, results in small pore throats that are commonly isolated. The sandstone is then cut by very low porosity and permeability calcite-rich laminae, further impeding potential flow. Together these characteristics lead to the Fly Flat Member being deemed low permeability and therefore unsuitable for geosequestration.

Samphire Marsh Member (1175.2 – 1383.3 m)

A representative section of core near the top of the Samphire Marsh Member is shown in Appendix 5, with representative core images, corresponding petrographic studies, and the core-measured porosity and permeability. The Samphire Marsh Member is dominated by mudstone with carbonate nodules and mudstone interbedded with limestone. It has end point compositions of 100% mudstone, composed of detrital clay and micrite, and 100% limestone demonstrated by wireline log response, with a continuum between these end points (Fig. 15). Limestone in this member ranges from wackestone at the top to packstone through the lower half (Normore et al., 2017).

The average volume of clay interpreted from wireline logs ranges from 5 to 52%. Micrite and other calcitic grains are undifferentiated in the petrophysical interpretation, represented as a summed volume of calcite, ranging from 10 to 94%. Quartz volume ranges from 0 to 39%. The wireline log interpretation of these volumes has been calibrated to core using XRD results (Normore et al., 2017) to calculate mineral volumes (Fig. 16a–d). Dolomite has also been estimated from logs; however, this volume has not undergone the same rigorous calibration to core.

Fourteen samples were analysed for routine core analysis in the Samphire Marsh Member, two of which fractured during analysis with the remainder providing a porosity range of 1.4 to 8.3%. Core calibrated total porosity averaged just 3%, ranging from almost 0.5 to 18%. As the volume of clay increases, so does porosity (Fig. 17), demonstrating that micropores in detrital clays are the principal pore system. Primary and secondary porosity within the calcitic matrix has been occluded by carbonate cementation, as evidenced in both the neutron-density crossplot (Fig. 15) and petrographicwork (Normore et al., 2017), with the porous network best viewed in SEM photography (Fig. 18). A paragenetic sequence based on crosscutting relationships of the diagenetic components observed in thin section has been proposed by Dent et al. (2021b; Fig. 19).

Mud gas peaked at the top of the Samphire Marsh Member, coinciding with microporous mudstones where porosity is best preserved. However, no hydrocarbons have been interpreted from resistivity using the Archie equation, with the interval expected to be water filled.

Permeability is extremely poor in the Samphire Marsh Member, with no routine core analysis measurements exceeding 1 mD. Experimental error associated with measuring permeability on plugs with less than 1 mD permeability is extremely high (Thomas and Pugh, 1987), hence no attempt has been made to build a permeability model based on these measurements. The mudstone intervals provide the best opportunity for development of a connected porous network, and therefore the greatest permeability. The mud gas peaks through the highest porosity mudstones support this theory; however, measured permeabilities and special core analysis studies (including mercury injection threshold pressure and flow studies measuring specific permeability to water and threshold pressure to CO_2 gas) demonstrate that this interval has low permeability and would be an effective seal for the underlying Fly Flat Member.

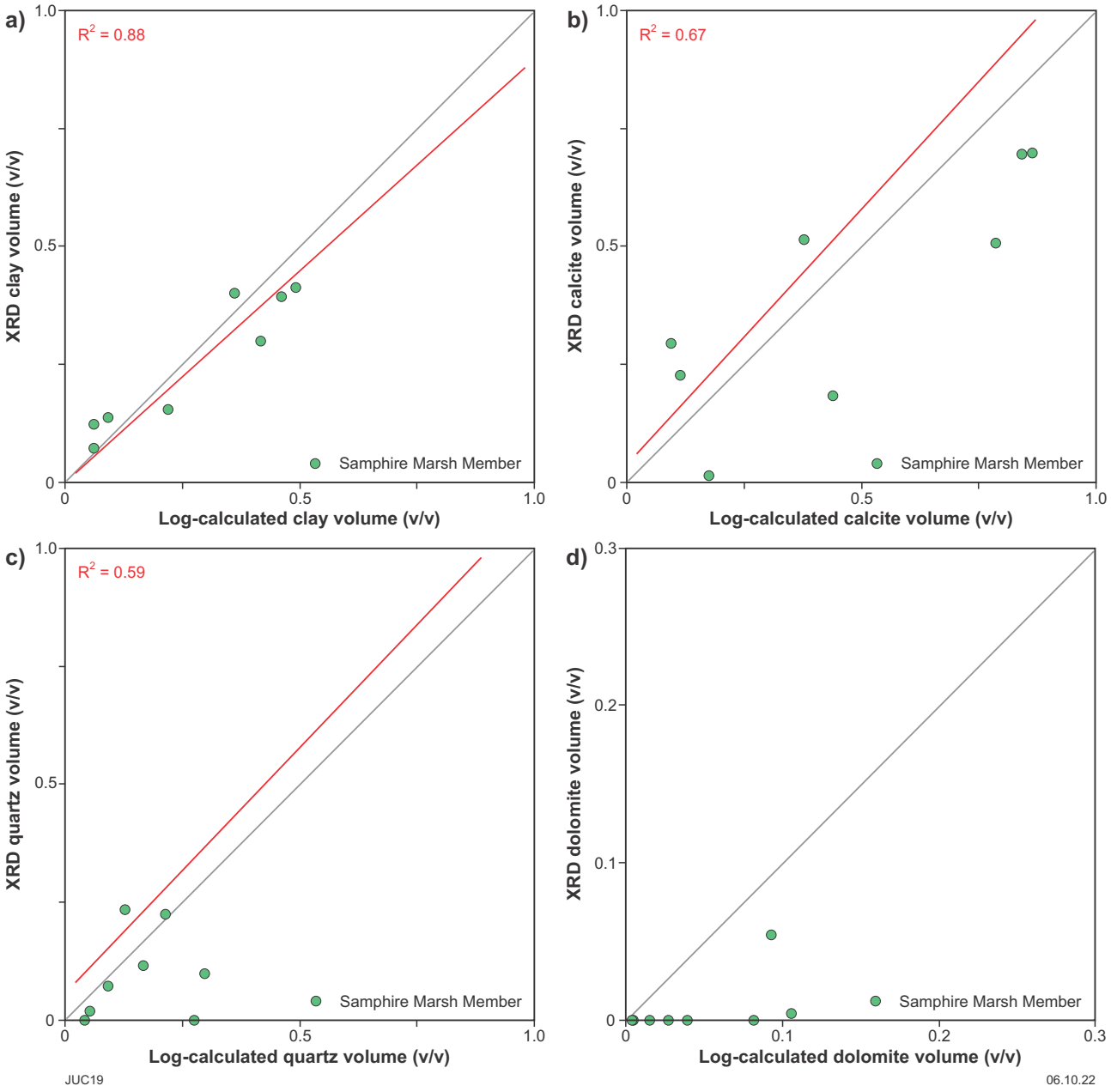

Figure 16. Comparison of XRD and log-derived mineral volumes: a) XRD total clay volume compared to log-estimated total clay volume; b) XRD calcite volume compared to log-estimated calcite volume; c) XRD quartz volume compared to log-estimated quartz volume; d) XRD dolomite volume compared to log-estimated dolomite volume

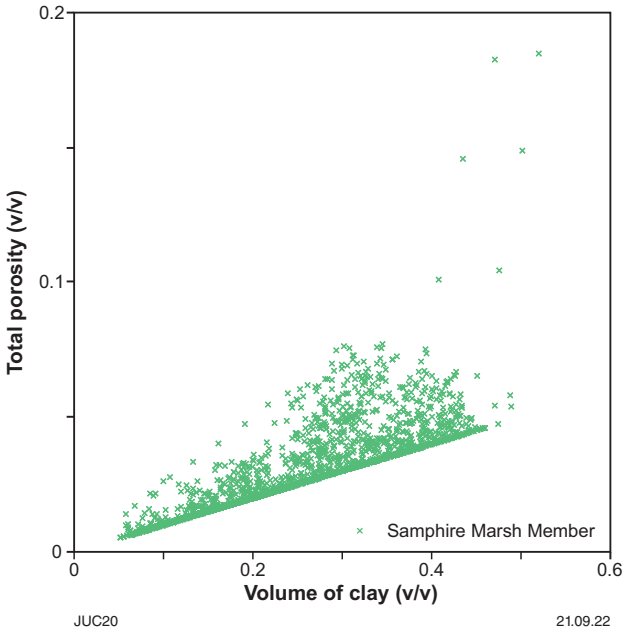

Figure 17. Crossplot showing log-derived total porosity increasing as the total volume of clay increases, demonstrating micropores in detrital clays are the principal pore system

To determine the seal potential for geosequestration of the Samphire Marsh Member, further studies should be conducted to understand the distribution of the high porosity mudstone facies and how the mechanical properties of mudstone and limestone differ within this unit.

Willara Formation (898 – 1175.2 m)

The Willara Formation is 277.2 m thick in Olympic 1, but only the basal 47.5 m has been cored. With limited core data points, wireline interpretation of the Willara Formation has been assessed to further understand reservoir quality controls that may impact Willara Formation reservoir potential elsewhere in the basin.

A study of thin sections, SEM, CL and XRD reveal present-day porosity is limited to micropores mainly distributed among micritic calcite crystals (Petrography report in Normore and Dent, 2017). Routine core analysis of three samples at the base of the Willara Formation revealed porosity values from 0.2 to 2.2%. The micropores in these plugs are poorly connected, resulting in very low measured permeability (less than 0.001 mD; Fig. 3). Cathodoluminescence indicates early marine calcite cements have destroyed most primary and secondary porosity, with further losses due to burial as the early calcite cements and calcitic matrix have simultaneously recrystallized and stabilized (Fig. 20). Minor bitumen fills intercrystal pores in cemented vugs, indicating late hydrocarbon migration (Fig. 21).

The very top of the Willara Formation (outside of the cored interval) has been dolomitized. This zone was the reservoir target for the well as dolomitization commonly creates secondary porosity capable of hosting commercial hydrocarbon accumulations. A neutron-density crossplot (Fig. 22) readily differentiates a 10-m thick dolomite interval from the underlying limestone.

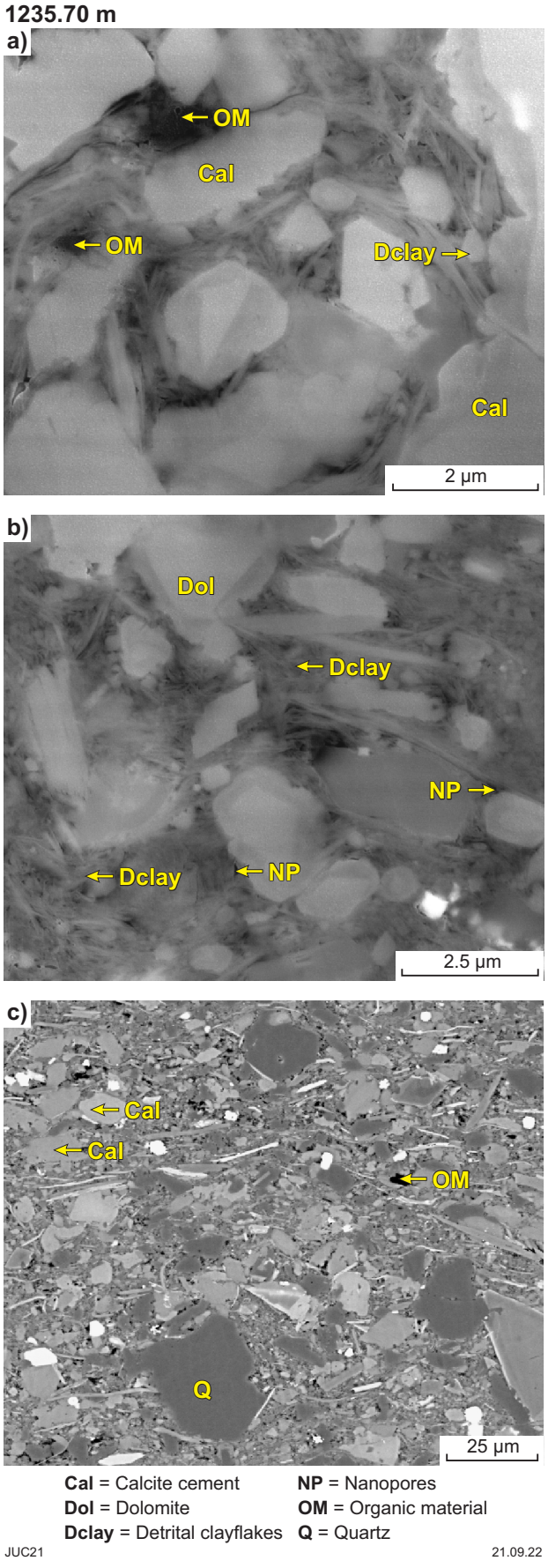

Figure 18. AR-ion milled SEM petrography showing nanopores in detrital clays: a) high-resolution image showing the occurrence of organic material, calcite, detrital clay and nanoporosity; b) high-resolution image showing the presence of nanopores between clay flakes; c) relatively low-magnification view showing the detailed texture of this calcareous claystone

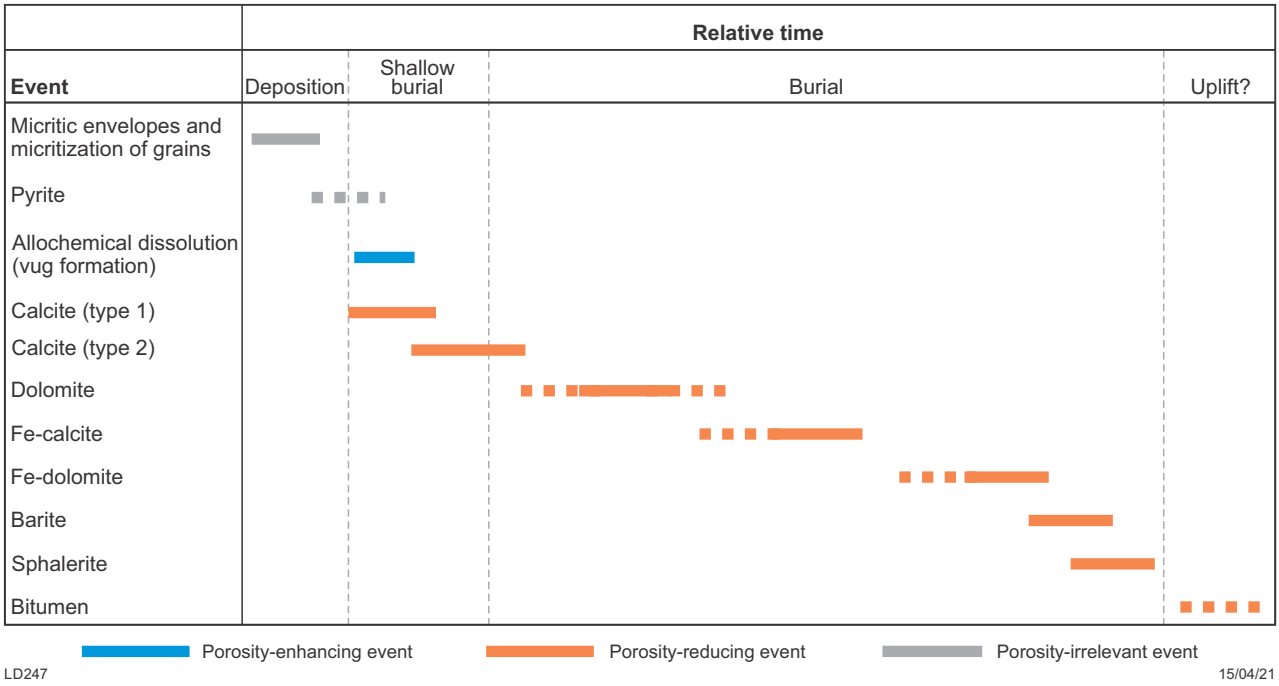

Figure 19. Samphire Marsh Member paragenetic sequence derived from thin sections (Dent et al., 2021b)

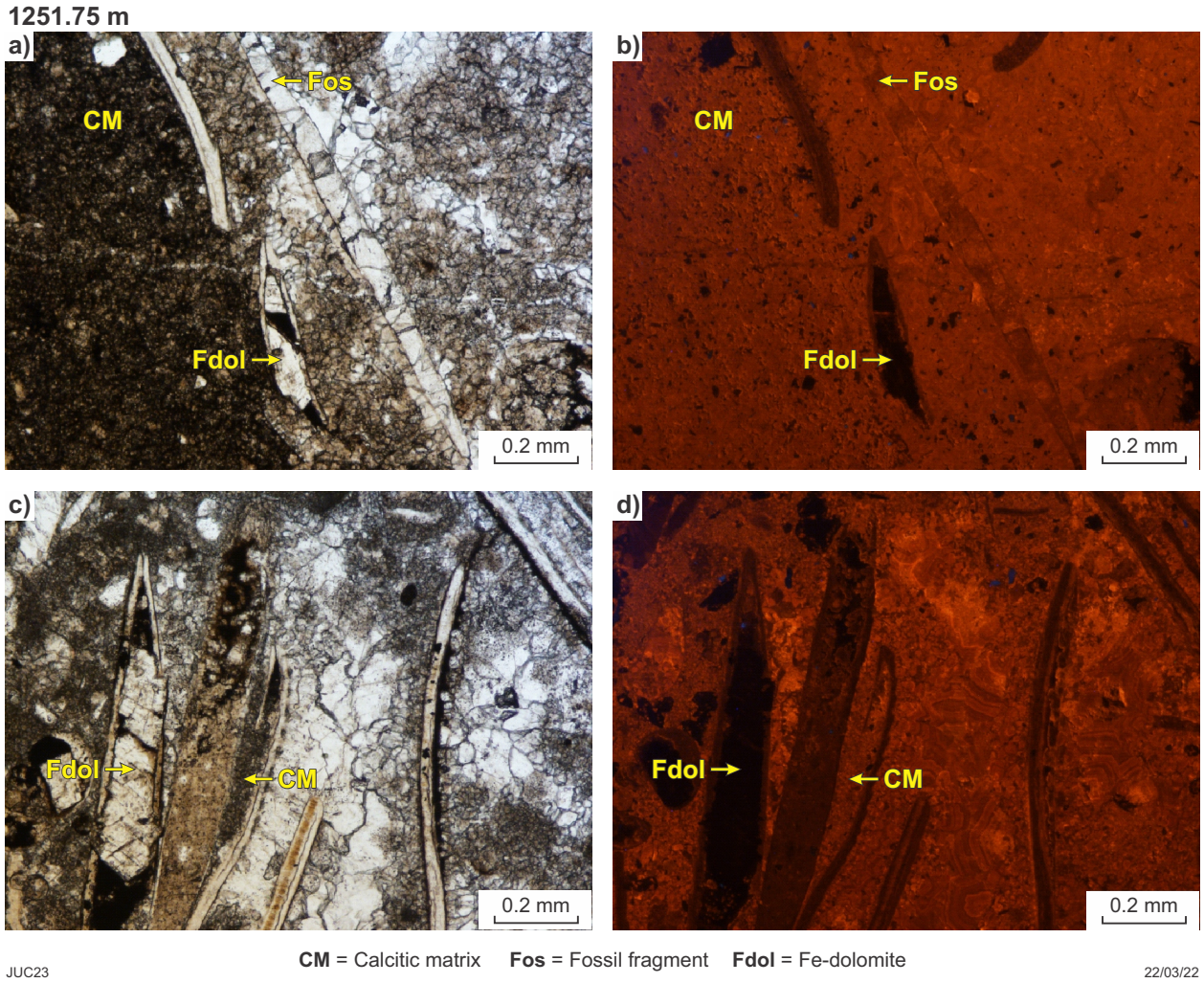

Figure 20. Cathodoluminescence photomicrograph showing marine cements: a) plane light view of limestone with abundant calcitic matrix, calcite cement, fossil fragments and Fe-dolomite occluded intraskeletal pores; b) cathodoluminescence view of (a); c) plane light view of limestone with abundant calcite cements, minor calcitic matrix and Fe-dolomite occluded intraskeletal pores; d) cathodoluminescence view of (c)

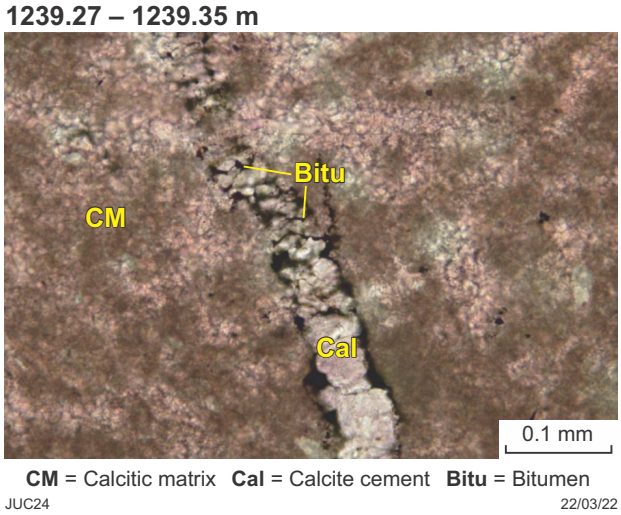

Figure 21. Thin section showing the occurrence of residual bitumen in cemented vugs

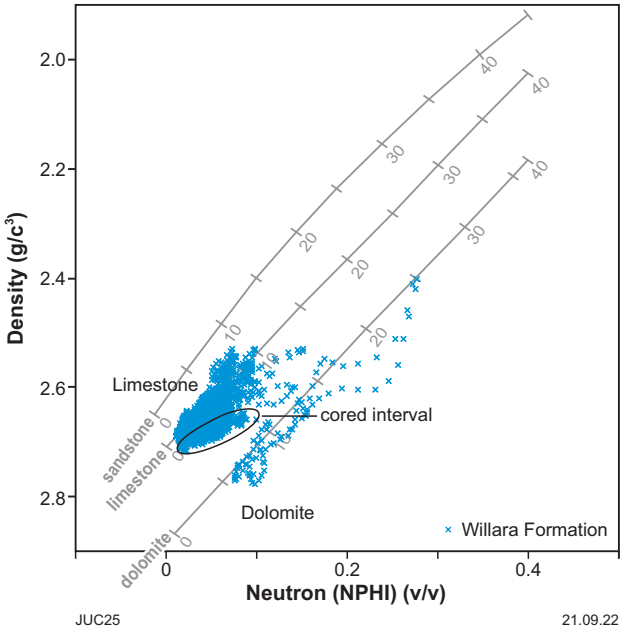

Figure 22. Willara Formation neutron-density crossplot (Weatherford, 2007) with mineral-specific porosity overlays demonstrating dolomites, intersected at the top of the Willara Formation, have higher porosity than limestones

Some porosity creation is associated with the dolomitization, spiking to 19.5% and averaging 5.1% total porosity compared to 1.5 – 2.5% in the limestone below. The cored Willara Formation interval is also highlighted on this crossplot, showing the cored interval has a slightly stronger shale effect than the uncored limestone, representing a gradual change from limestone to lime mudstone.

Poor to very poor oil shows are common in the Willara Formation. These observations appear to be associated with residual bitumen, with the Archie resistivity interpretation confirming the interval is close to 100% water filled.

Limestone matrix permeability measured on core plugs at the base of the Willara Formation are less than 0.01 mD; all rocks with less than 3% porosity are expected to have similar or lower permeability. Zones with porosity much greater than 3%, like the top 10 m of dolomite, should have higher permeabilities if the dolomitization is extensive and the associated vuggy porosity interconnected.

Grant Group (433.5 – 898 m)

The Grant Group consists of fluvio-deltaic and glacigene facies. It was intersected from 433.5 to 898 m MD, with a full suite of wireline logs acquired from 700 m MD. In the logged interval, the basal part of the group is dominantly claystone overlain by calcareous sandstone. Both facies are interpreted to include diamictites (Buru Energy Limited, 2015b), containing mostly granitic clasts. The reference to claystone here indicates grain size rather than clay mineralogy, with interpreted average volume of clay approximately 18% throughout (Fig. 23). The calcareous sandstone has excellent reservoir properties, with an average total porosity of 27.8%. The claystone has good reservoir properties, with an average total porosity of 16.8%. Total porosity drops through diamictites to approximately 15.7% as the clasts contribute little overall porosity.

A single oil show was recorded through this interval, with wireline interpretation confirming the interval is close to 100% water filled.

No permeability has been measured or estimated for this interval, although the grain size change between calcareous sandstone to claystone is expected to be accompanied by a significant drop in permeability because the average pore throat size is expected to be a major control on permeability (Pittman, 1992).

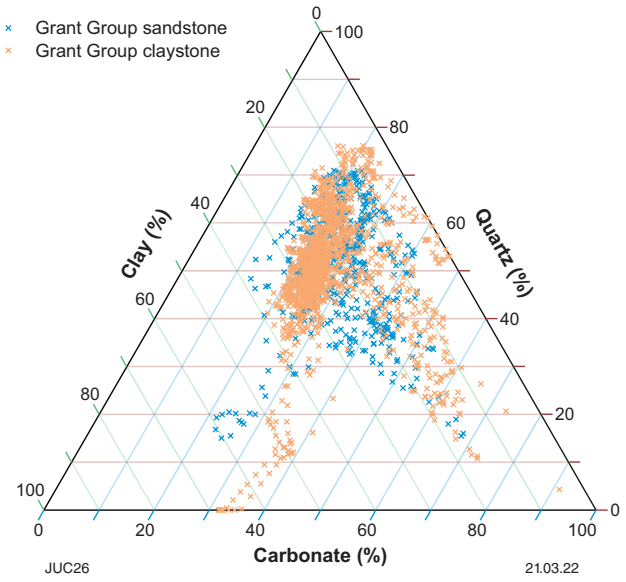

Figure 23. Sandstone and claystone facies have comprehensive wireline log coverage in the Grant Group. This ternary diagram shows that mineral assemblage remains relatively unchanged as the grain size is dramatically reduced moving from sandstone to claystone, indicating grain size as the main control on reservoir quality

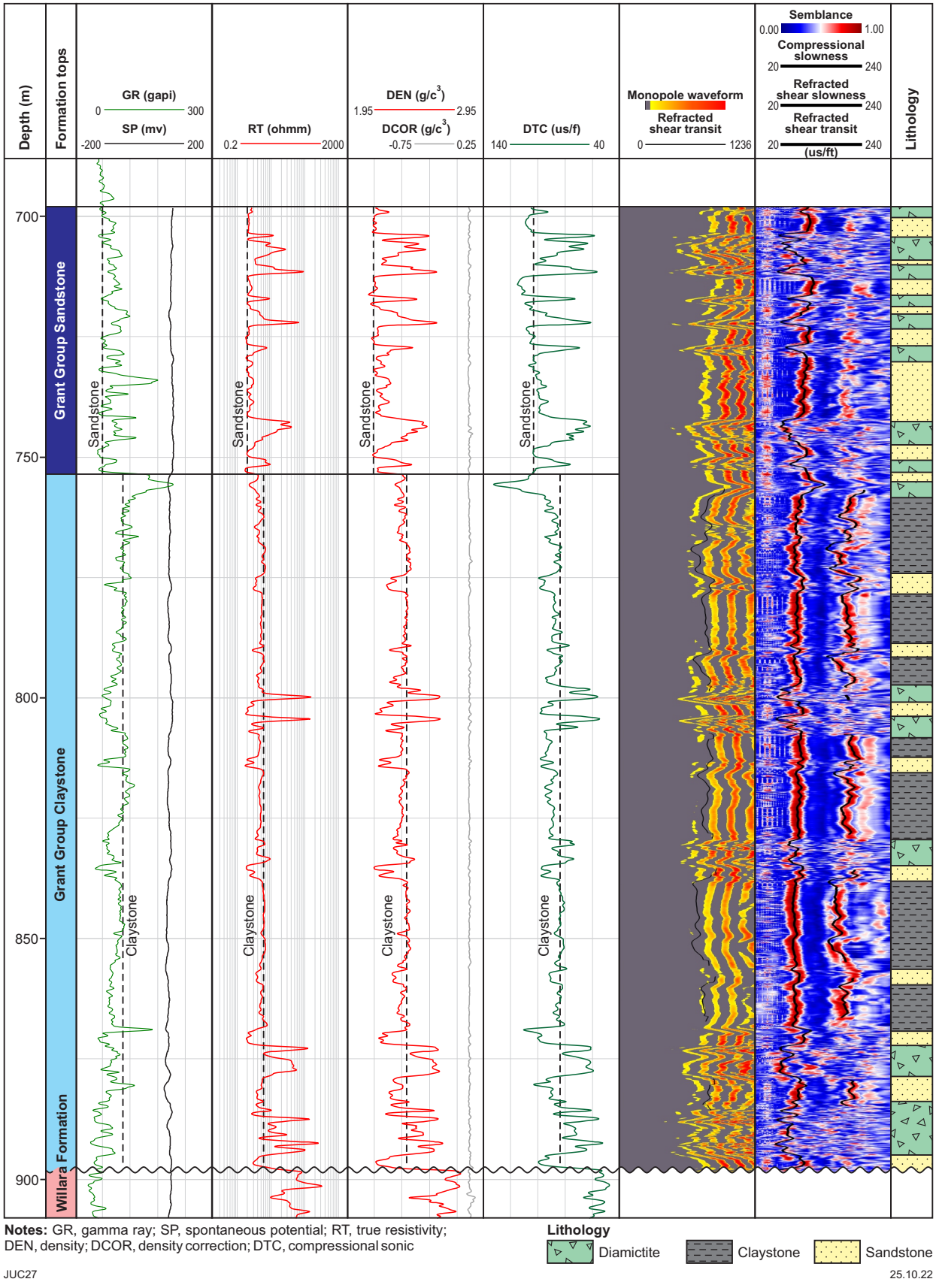

Figure 24. Log properties of calcareous sandstone (698 – 753.5 m) and claystone (753.5 – 898 m) facies in the Grant Group with recorded waveforms and semblance data showing poor coherency of compressional and shear arrivals through diamict intervals, demonstrating the contrasting acoustic properties of the matrix and clasts

Olympic 1 was prognosed to intersect the Goldwyer Formation below the Meda unconformity, based on interpretation of seismic data. However, the Goldwyer Formation was not present below the Meda unconformity. Consequently, the carbonate target within the Willara Formation lacked a seal. The petrophysical characteristics of the rock types directly overlying the unconformity were examined to reveal why these Permian and Ordovician units have a similar seismic character.

The lithology change from calcareous sandstone to claystone coincides with the prognosed Meda unconformity pre-drill interpretation. When drilling through this lithology change the mud logging team predicted the top of the Goldwyer Formation but noted that cuttings contained a higher proportion of sandstone than expected and lacked limestone (Buru Energy Limited, 2015a). Wireline logging later confirmed the lithology change to be a quartz-rich claystone rather than carbonaceous shale and therefore verified the absence of the Goldwyer Formation.

Average properties of the calcareous sandstone matrix (698 – 753.5 m) and claystone (753.5 – 898 m) are represented with blocked curves in Figure 24. Log response in diamictite intervals deviate strongly from these average matrix values, as they are dominated by clasts. Examples of cored diamictites in the Grant Group elsewhere in the basin are shown in Mory et al., 2008.

Semblance plots over the diamictite intervals (Fig. 24) are characterized by very poor coherency because each arrival recorded travels through different volumes of matrix and clasts, and although the average travel times are faster, it is conceivable that seismic-scale rock properties would replicate the matrix rock properties. Averaged matrix properties have therefore been used for comparison with the Goldwyer Formation shale properties to understand how the Grant Group claystone can have similar seismic character to the Goldwyer Formation shale.

Acoustic impedance was calculated from the compressional sonic and density measurements for Olympic 1 and Thangoo 2. Thangoo 2 intersects Goldwyer Formation at the Meda unconformity at a similar depth to the prognosed Goldwyer Formation in Olympic 1. The crossplot of the acoustic impedance against depth compares this formation with the Grant Group (Fig. 25). Both show similar acoustic impedance within carbonaceous shale of the Goldwyer Formation and the claystone in the Grant Group. The lack of acoustic impedance contrast between the Goldwyer Formation and the Grant Group claystone explains the ambiguity in mapping the Meda unconformity between these units in this area.

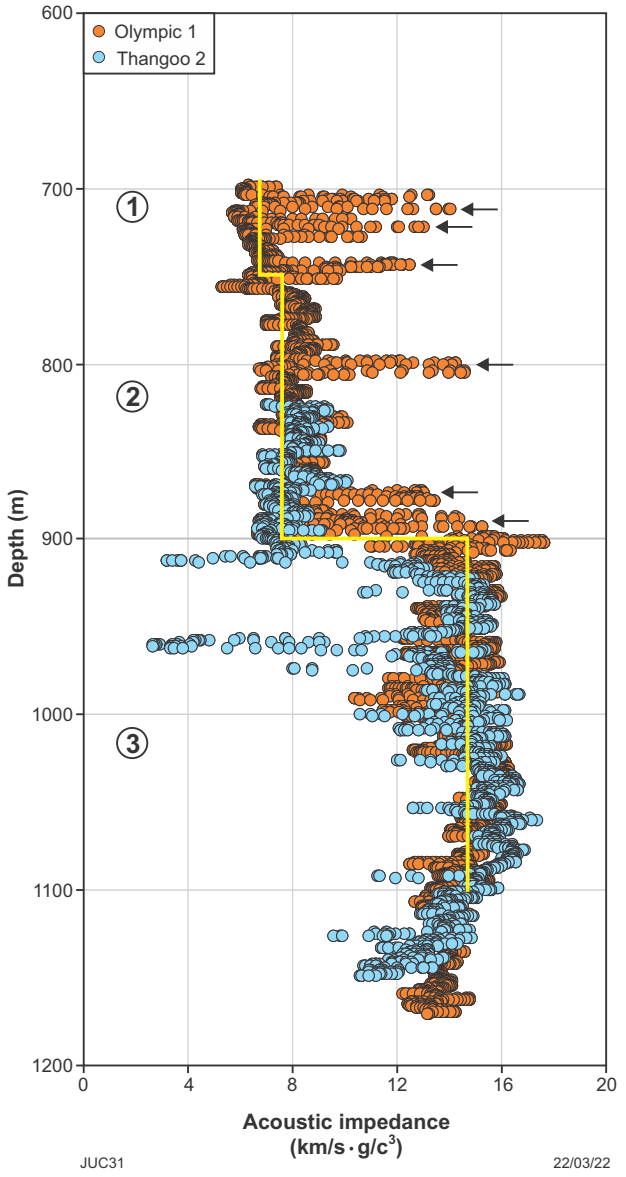

Figure 25. Acoustic impedance at Thangoo 2 and Olympic 1: 1) Solid yellow curve depicting the matrix acoustic impedance of the calcareous sandstone in the Grant Group at Olympic 1. Arrows highlighting thin diamictites that deviate from matrix acoustic impedance, where the acoustic impedance calculated at log scale is dominated by clasts within the diamictite; 2) Solid yellow curve depicting the matrix acoustic impedance of the claystone facies in the Grant Group at Olympic 1 and Goldwyer Formation shales at Thangoo 2. No seismically mappable event is expected between Grant Group claystone and Goldwyer Formation; 3) Willara Formation at Olympic 1 and Thangoo 2. Identical acoustic impedance contrast going from the Grant Group claystone to Willara Formation and Goldwyer Formation to Willara Formation

Conclusions

Although petrophysical evaluation of the Fly Flat Member reveals good porosity and therefore good reservoir storage capacity, the prevalence of calcite-rich laminations, quartz overgrowths and calcite precipitation has isolated much of the macroporisty. Permeability is generally less than 0.1 mD in the very fine and fine-grained rocks, improving to 0.1 – 13.4 mD in the medium-grained rocks, limiting hydrocarbon and carbon sequestration reservoir potential.

The petrophysical characteristics of the Samphire Marsh Member indicate that while this unit is uniformly microporous, it comprises a heterogeneous mix of mudstone and limestone with very different reservoir properties, whose mechanical properties need to be studied before proposing this formation as a seal for geosequestration.

The Willara Formation is capped by a distinct dolomitized zone that has enhanced porosity and permeability. The occurrence of an oil show in this interval also indicates the validity of the upper Willara Formation as a potential hydrocarbon target elsewhere in the Canning Basin.

Seismic interpretation of future Goldwyer Formation prospects would benefit from a regional understanding of the Meda unconformity and the imperceptible seismic contrast that occurs between the Grant Group claystone and Goldwyer Formation mudstone.

Acknowledgements

Arthur Mory and Alex Zhan are thanked for their guidance during this work.

References

Archie, GE 1952, Classification of carbonate reservoir rocks and petrophysical considerations: AAPG Bulletin, v. 36, no. 2, p. 218–298.

Backhouse, J and Mory, AJ 2020, Mid-Carboniferous – Lower Permian palynology and stratigraphy, Canning Basin, Western Australia: Geological Survey of Western Australia, Report 207, 133p.

Buru Energy Limited 2015a, Olympic 1 well completion report, volume 1 – documentary data: Geological Survey of Western Australia, Statutory petroleum exploration report W21660 A1, 556p.

Buru Energy Limited 2015b, Olympic 1 well completion report, volume 2 – derivative data: Buru Energy: Geological Survey of Western Australia, Statutory petroleum exploration report W21660 A2, 78p.

Dent, L, Normore, L, Sullivan, NB, Zhen, YY and Forbes, A 2021a, First record of lower – Middle Ordovician (Tremadocian – Dapingian) carbon isotope ($\delta^{13}C_{carb}$) chemostratigraphy in the Canning Basin, Western Australia; calibrated with geochronology/biostratigraphy and implications for global correlations: Palaeogeography, Palaeoclimatology, Palaeoecology, v. 573, article no. 110411, 12p., doi:10.1016/j.palaeo.2021.110411.

Dent, LM and Normore, LS 2017, Assessment of thermal maturity using bitumen, graptolite, and bioclast reflectance: Ordovician Nambeet Formation, Canning Basin: Geological Survey of Western Australia, Report 170, 1111p.

Dent, LM, Normore, LS and Martin, SK 2021b, Reference section, revised stratigraphy and facies analysis of the Ordovician Nambeet Formation, Canning Basin, Western Australia: Geological Survey of Western Australia, Report 211, 75p.

Dunham, RJ 1962, Classification of carbonate rocks according to depositional texture, *in* Classification of carbonate rocks *edited by* WE Hamm: American Association of Petroleum Geologists, Tulsa, Oklahoma, USA, p. 108–121.

Folk, RL 1980, Petrology of sedimentary rocks: Hemphill Publishing Company, Austin, Texas, USA, 182p.

Ghori, KAR 2013, Petroleum geochemistry and petroleum systems modelling of the Canning Basin, Western Australia: Geological Survey of Western Australia, Report 124, 33p.

International Commission on Stratigraphy (compiler) 2013, International chronostratigraphic chart – v2016/10 update: The ICS international chronostratigraphic chart, 199–204.

Kennard, JM, Jackson, MJ, Romine, KK, Shaw, RD and Southgate, PN 1994, Depositional sequences and associated petroleum systems of the Canning Basin, WA, *in* The Sedimentary Basins of Western Australia *edited by* PG Purcell and RR Purcell: Petroleum Exploration Society of Australia: West Australian Basins Symposium, Perth, Western Australia, 14–17 August 1994, p. 657–676.

Mory, AJ, Redfern, J and Martin, JR 2008, A review of Permian–Carboniferous glacial deposits in Western Australia, *in* Resolving the late Paleozoic Ice Age in time and space *edited by* CR Fielding, TD Frank and JL Isbell: Geological Society of America, Boulder, Colorado, USA, Special Paper 441, p. 29–40, doi:10.1130/2008.2441(02).

Normore, L, Haines, PW, Carr, LK, Henson, P, Zhan, Y, Wingate, MTD, Zhen, YY, Lu, Y, Martin, S, Kelsey, D, Allen, H and Fielding, I 2021, Barnicarndy Graben, southern Canning Basin: stratigraphy defined by the Barnicarndy 1 stratigraphic well: The APPEA Journal, v. 61, no. 1, p. 224–235, doi:10.1071/AJ20160.

Normore, LS and Dent, LM 2017, Petroleum source potential of the Ordovician Nambeet Formation, Canning Basin: Evidence from petroleum well Olympic 1: Geological Survey of Western Australia, Report 169, 20p.

Normore, LS, Dent, LM and Symonds, AK 2017, Olympic 1, Canning Basin: Geological Survey of Western Australia: Digital Core Atlas Series, 212p., <www.dmirs.wa.gov.au/wapims>.

Normore, LS, Zhen, YY, Dent, LM, Crowley, JL, Percival, IG and Wingate, MTD 2018, Early Ordovician CA-IDTIMS U–Pb zircon dating and conodont biostratigraphy, Canning Basin, Western Australia: Australian Journal of Earth Sciences, v. 65, p. 61–73, doi:10.1080/08120099.2018.1411292.

Pickett, GR 1973, Pattern recognition as a means of formation evaluation: The Log Analyst, v. 14, no. 4, p. 3–11, <https://onepetro.org/petrophysics/article-abstract/171683/Pattern-Recognition-As-A-Means-Of-Formation?redirectedFrom=fulltext>.

Pittman, ED 1992, Relationship of porosity and permeability to various parameters derived from mercury injection—capillary pressure curves for sandstone (1): American Association of Petroleum Geologists Bulletin, v. 76, no. 2, p. 191–198.

Shaw, RD, Sexton, M and Zeilinger, I 1995, The tectonic framework of the Canning Basin, WA, including 1:2 million structural elements map of the Canning Basin: Geoscience Australia, Record 1994/48, 89p.

Thomas, D and Pugh, V (compilers) 1987, A statistical analysis of the accuracy and reproducibility of standard core analysis; SCA Annual Conference: Dallas, TX, USA: Society of Special Core Analysts, SCA paper 8701.

Weatherford 2007, Log Interpretation Charts: Compact™ Tool Series: Weatherford, Houston, Texas, Document no. 4060.01, 66p. (unpublished).

Winsauer, WO and Shearin, HM 1952, Resistivity of brine-saturated sands in relation to pore geometry: AAPG Bulletin, v. 36, p. 253–277, doi:10.1306/3D9343F4-16B1-11D7-8645000102C1865D.

Zhen, YY, Nicoll, RS, Normore, LS, Percival, IG, Laurie, JR and Dent, LM 2020, Ordovician conodont biostratigraphy of the Willara Formation in the Canning Basin, Western Australia: Palaeoworld, v. 30, no. 2, p. 249–277, doi:10.1016/j.palwor.2020.06.006.

Appendix 1

Stratigraphic column of the Canning Basin

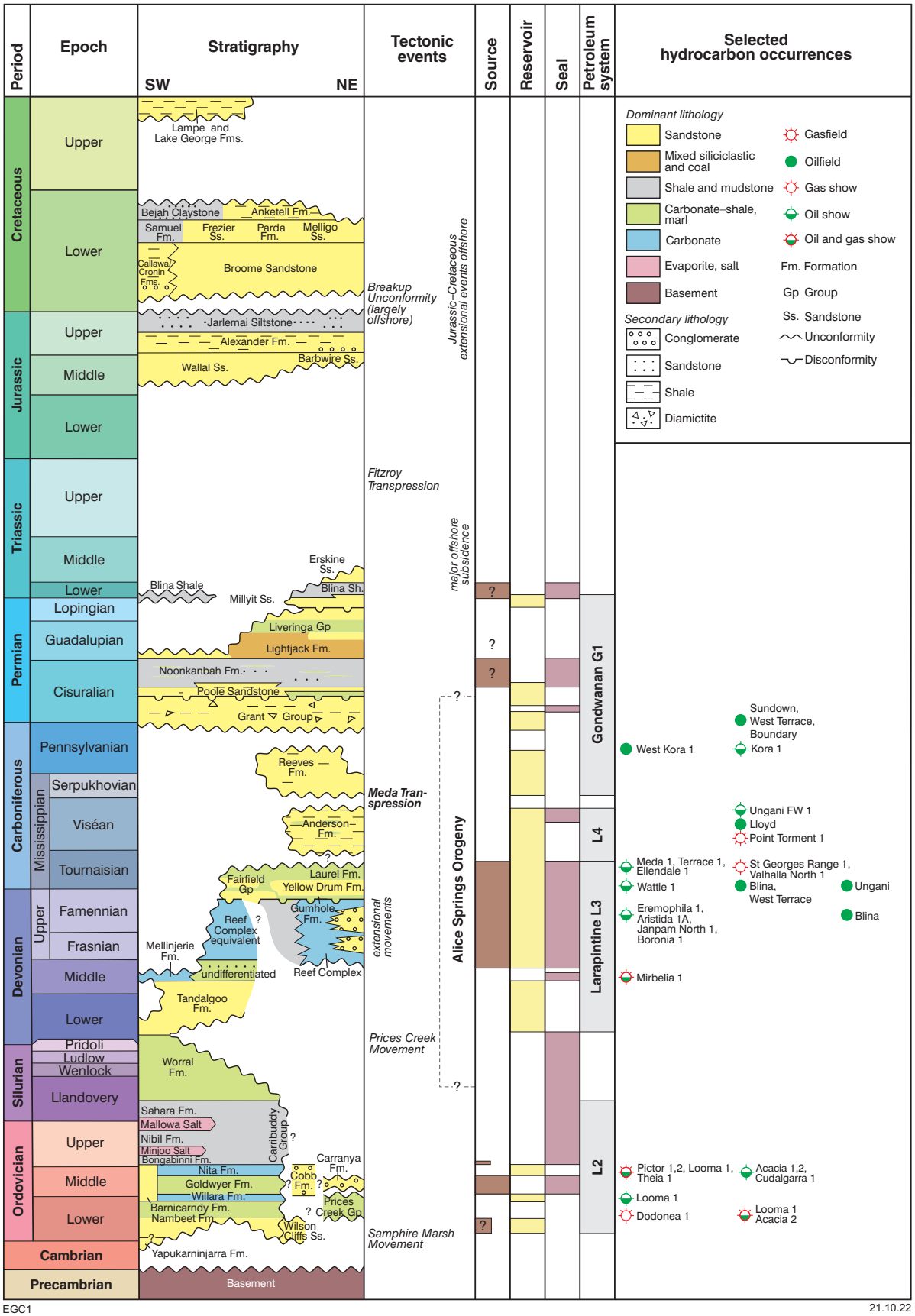

Figure 1.1. Stratigraphic column of the Canning Basin showing lithostratigraphic units, tectonic events according to Shaw et al. (1995), elements of the petroleum system and known hydrocarbon occurrences

Appendix 2

Petrographic analytical program and sample summary

Formation	*Sample*	*Depth*	*TS*	*SEM*	*AIM-SEM*	*CL*	*XRD*	*Lithology*	*Classification*
Willara Formation	221483	1128.28	X					Limestone	Wackestone
	221482	1128.41	X	X		X	X	Limestone	Wackestone
	221484	1134.57	X					Limestone	Wackestone
	216071	1146.65	X	X			X	Argillaceous dolomitic limestone	Lime mudstone
	221485	1153.29	X	X		X	X	Limestone	Wackestone
	216072	1175.38	X	X			X	Silty dolomitic calcareous claystone	
Samphire Marsh Member	216073	1183.07	X	X			X	Silty calcareous claystone	
	221500	1188.43	X			X		Limestone	Lime mudstone
	216074	1192.39	X	X			X	Silty calcareous claystone	
	216075	1200.63	X		X		X	Dolomitic calcareous claystone	
	216076	1213.12	X	X			X	Silty dolomitic dalcareous claystone	
	216078	1235.70	X		X		X	Calcareous claystone	
	216078	1235.86	X	X			X	Silty calcareous claystone	
	216080	1239.30	X					Dolomitic limestone	Wackestone
	216079	1244.35	X	X			X	Silty calcareous claystone	
	221499	1251.78	X	X		X	X	Limestone	Packstone
	221486	1363.06	X					Altered volcanic rock	
	221801	1294.88	X					Limestone	Wackestone
	216081	1311.17	X		X		X	Dolomitic claystone	
	221497	1317.02	X					Altered volcanic rock	
	221487	1337.83	X					Limestone	Packstone
	221802	1339.30	X			X		Limestone	Packstone/grainstone
	221498	1343.07	X	X		X	X	Argillaceous limestone	Packstone/grainstone
	216082	1355.29	X		X		X	Dolomitic claystone	
	221488	1365.07	X	X		X	X	Argillaceous limestone	Wackestone
	221803	1369.94	X			X		Limestone	Grainstone
	221489	1375.02	X	X			X	Argillaceous limestone	Wackestone/packstone
	221490	1383.25	X					Glauconitic argillaceous limestone	Wackestone/packstone
Fly Flat Member	221807	1386.08	X	X		X	X	Sandstone	Subarkose
	221492	1393.40	X	X			X	Sandstone	Subarkose
	221493	1393.54	X	X		X	X	Sandstone	Subarkose
	221495	1393.72	X	X			X	Sandstone	Subarkose
	221807	1397.08	X	X			X	Sandstone	Subarkose
	221808	1404.11	X	X		X	X	Sandstone	Subarkose
	221805	1406.92	X	X			X	Sandstone	Subarkose
	221804	1417.07	X					Calcareous sandstone	Subarkose
	221809	1420.11	X	X		X	X	Sandstone	Subarkose
	221806	1425.21	X					Calcareous sandstone	Subarkose
	221810	1427.11	X	X		X	X	Calcareous sandstone	Subarkose
	221811	1427.92	X	X		X	X	Sandy limestone	Packstone
	221812	1430.53	X	X		X	X	Sandstone	Subarkose
	221813	1434.73	X	X		X	X	Calcareous sandstone	Subarkose
	221814	1443.16	X	X		X	X	Sandstone	Subarkose
	221815	1447.37	X	X		X	X	Sandstone	Subarkose

Notes: TS, thin section; SEM, scanning electron microscopy; AIM-SEM, argon ion milled scanning electron microscopy; CL, cathodoluminescence microscopy; XRD, X-ray diffraction analysis

Appendix 3

Routine core analysis results with lithology descriptions

Fm	Sample	Depth (m)	$Perm_{inf}$ (mD)	$Perm_{air}$ (mD)	Porosity (%)	Grain density (g/cc)	Lithology	Classification	Comments
Willara Formation	221482	1128.41	0.00018	0.00132	2.2	2.697	Limestone	Wackestone	
	216071	1146.46	0.0000162	0.000241	1.9	2.701	Argillaceous dolomitic limestone	Wackestone	
	221485	1152.29	0.0000685	0.000663	0.2	2.701	Limestone	Wackestone	
	216072	1175.47	0.00737	0.0239	7	2.745	Silty dolomitic calcareous claystone	n/a	
Samphire Marsh Member	216073	1183.11				2.709	Silty calcareous claystone	n/a	Fractured
	216074	1192.44	0.0203	0.0521	4.9	2.677	Silty calcareous claystone	n/a	
	216075	1200.63	0.633	0.728	8.3	2.71	Dolomitic calcareous claystone	n/a	
	216076	1212.96	0.512	0.52	6.1	2.699	Silty dolomitic calcareous claystone	n/a	
	216077	1224.02	0.00138	0.00628	5.8	2.711	Silty calcareous claystone	n/a	
	216078	1235.7	0.00312	0.0121	3.5	2.655	Silty calcareous claystone	n/a	
	218078	1244.5	0.00411	0.0151	7.2	2.723	Silty calcareous claystone	n/a	
	221499	1251.78	0.000074	0.000681	1.4	2.709	Limestone	Packstone	
	216081	1311.17	0.0283	0.0686	8	2.699	Dolomitic claystone	n/a	
	221498	1343.07	0.0000816	0.000726	1.6	2.701	Argillaceous limestone	Packstone/grainstone	
	216082	1355.29	0.0697	0.141	7.8	2.709	Dolomitic claystone	n/a	
	221488	1365.07	0.363	0.408	3.1	2.708	Argillaceous limestone	Packstone/grainstone	
	221489	1375.02				2.715	Argillaceous limestone	Wackestone/packstone	Fractured
	221491	1386.08	12.3	13.7	15.9	2.634	Glauconitic argillaceous limestone	Wackestone/packstone	
Fly Flat Member	221492	1393.4	0.0751	0.14	12.6	2.642	Sandstone	Subarkose	
	221493	1393.54	0.0675	0.13	13.1	2.635	Sandstone	Subarkose	
	221495	1393.72	0.0402	0.0764	10.9	2.632	Sandstone	Subarkose	
	221807	1397.08	0.00291	0.0114	8	2.652	Sandstone	Subarkose	
	221808	1404.11	0.0131	0.0242	10.7	2.655	Sandstone	Subarkose	
	221805	1406.92	0.0504	0.106	11.4	2.652	Sandstone	Subarkose	
	221809	1420.11	0.00265	0.0106	9	2.645	Sandstone	Subarkose	
	221810	1427.11	0.000755	0.00397	3.53	2.653	Calcareous sandstone	Subarkose	
	221811	1427.92	0.0136	0.024	2	2.691	Sandy limestone	Packstone	
	221812	1430.53	0.00601	0.01	7.1	2.652	Sandstone	Subarkose	
	221813	1434.73	0.0314	0.0695	9.6	2.651	Calcareous sandstone	Subarkose	
	221814	1443.16	0.296	0.414	9.2	2.645	Sandstone	Subarkose	
	221815	1447.37	0.0131	0.0301	5.5	2.655	Sandstone	Subarkose	

Appendix 4

Core analysis describing typical lithologies in the Fly Flat Member

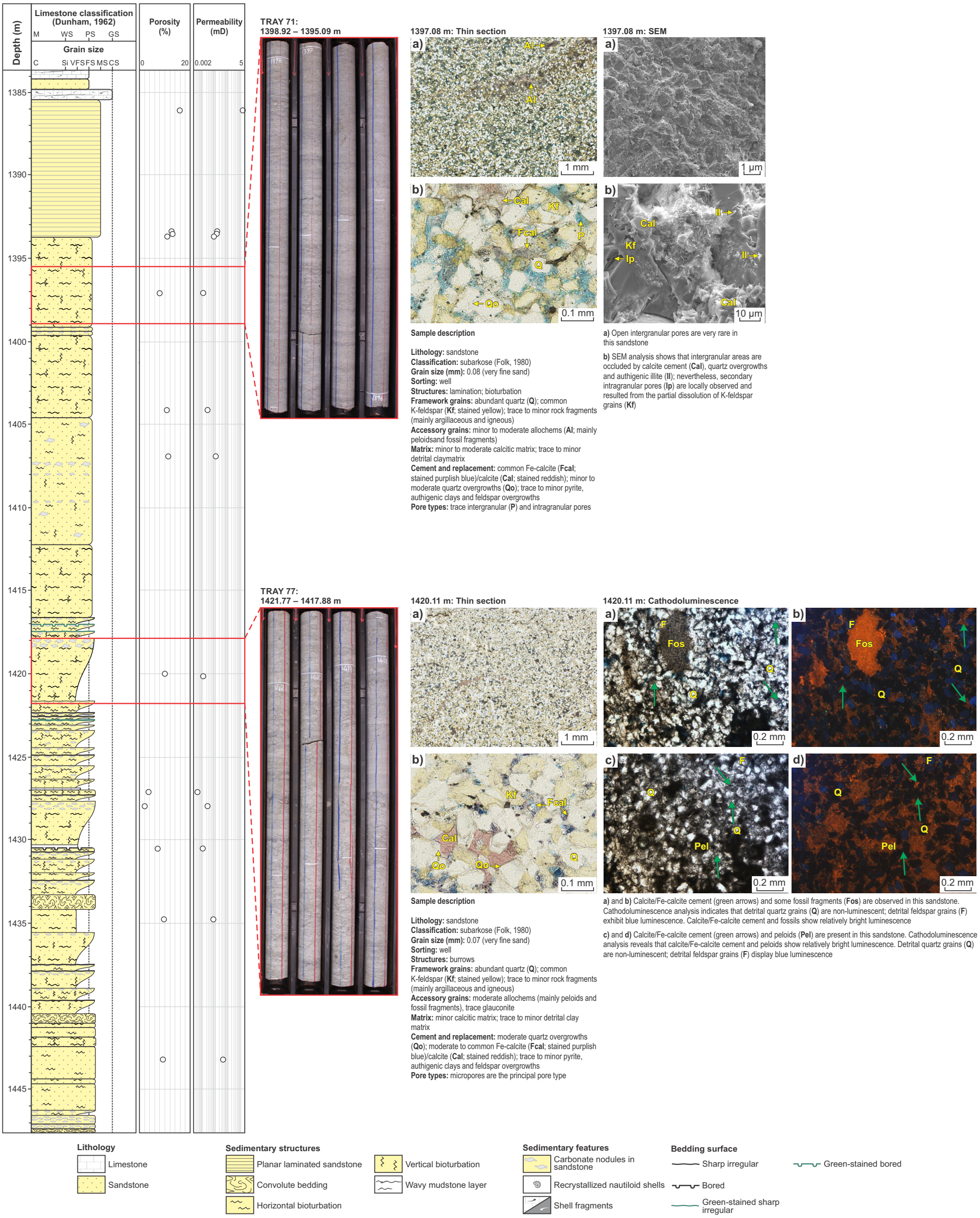

Sample description

Lithology: sandstone
Classification: subarkose (Folk, 1980)
Grain size (mm): 0.08 (very fine sand)
Sorting: well
Structures: lamination; bioturbation
Framework grains: abundant quartz (**Q**); common K-feldspar (**Kf**; stained yellow); trace to minor rock fragments (mainly argillaceous and igneous)
Accessory grains: minor to moderate allochems (**Al**; mainly peloidsand fossil fragments)
Matrix: minor to moderate calcitic matrix; trace to minor detrital claymatrix
Cement and replacement: common Fe-calcite (**Fcal**; stained purplish blue)/calcite (**Cal**; stained reddish); minor to moderate quartz overgrowths (**Qo**); trace to minor pyrite, authigenic clays and feldspar overgrowths
Pore types: trace intergranular (**P**) and intragranular pores

a) Open intergranular pores are very rare in this sandstone

b) SEM analysis shows that intergranular areas are occluded by calcite cement (**Cal**), quartz overgrowths and authigenic illite (**Il**); nevertheless, secondary intragranular pores (**Ip**) are locally observed and resulted from the partial dissolution of K-feldspar grains (**Kf**)

Sample description

Lithology: sandstone
Classification: subarkose (Folk, 1980)
Grain size (mm): 0.07 (very fine sand)
Sorting: well
Structures: burrows
Framework grains: abundant quartz (**Q**); common K-feldspar (**Kf**; stained yellow); trace to minor rock fragments (mainly argillaceous and igneous)
Accessory grains: moderate allochems (mainly peloids and fossil fragments), trace glauconite
Matrix: minor calcitic matrix; trace to minor detrital clay matrix
Cement and replacement: moderate quartz overgrowths (**Qo**); moderate to common Fe-calcite (**Fcal**; stained purplish blue)/calcite (**Cal**; stained reddish); trace to minor pyrite, authigenic clays and feldspar overgrowths
Pore types: micropores are the principal pore type

a) and **b)** Calcite/Fe-calcite cement (green arrows) and some fossil fragments (**Fos**) are observed in this sandstone. Cathodoluminescence analysis indicates that detrital quartz grains (**Q**) are non-luminescent; detrital feldspar grains (**F**) exhibit blue luminescence. Calcite/Fe-calcite cement and fossils show relatively bright luminescence

c) and **d)** Calcite/Fe-calcite cement (green arrows) and peloids (**Pel**) are present in this sandstone. Cathodoluminescence analysis reveals that calcite/Fe-calcite cement and peloids show relatively bright luminescence. Detrital quartz grains (**Q**) are non-luminescent; detrital feldspar grains (**F**) display blue luminescence

Figure 4.1. Core description with core-measured porosity and permeability and a selection of core photos and petrographic studies describing typical lithologies in the Fly Flat Member

Appendix 5

Core analysis describing typical lithologies in the Samphire Marsh Member

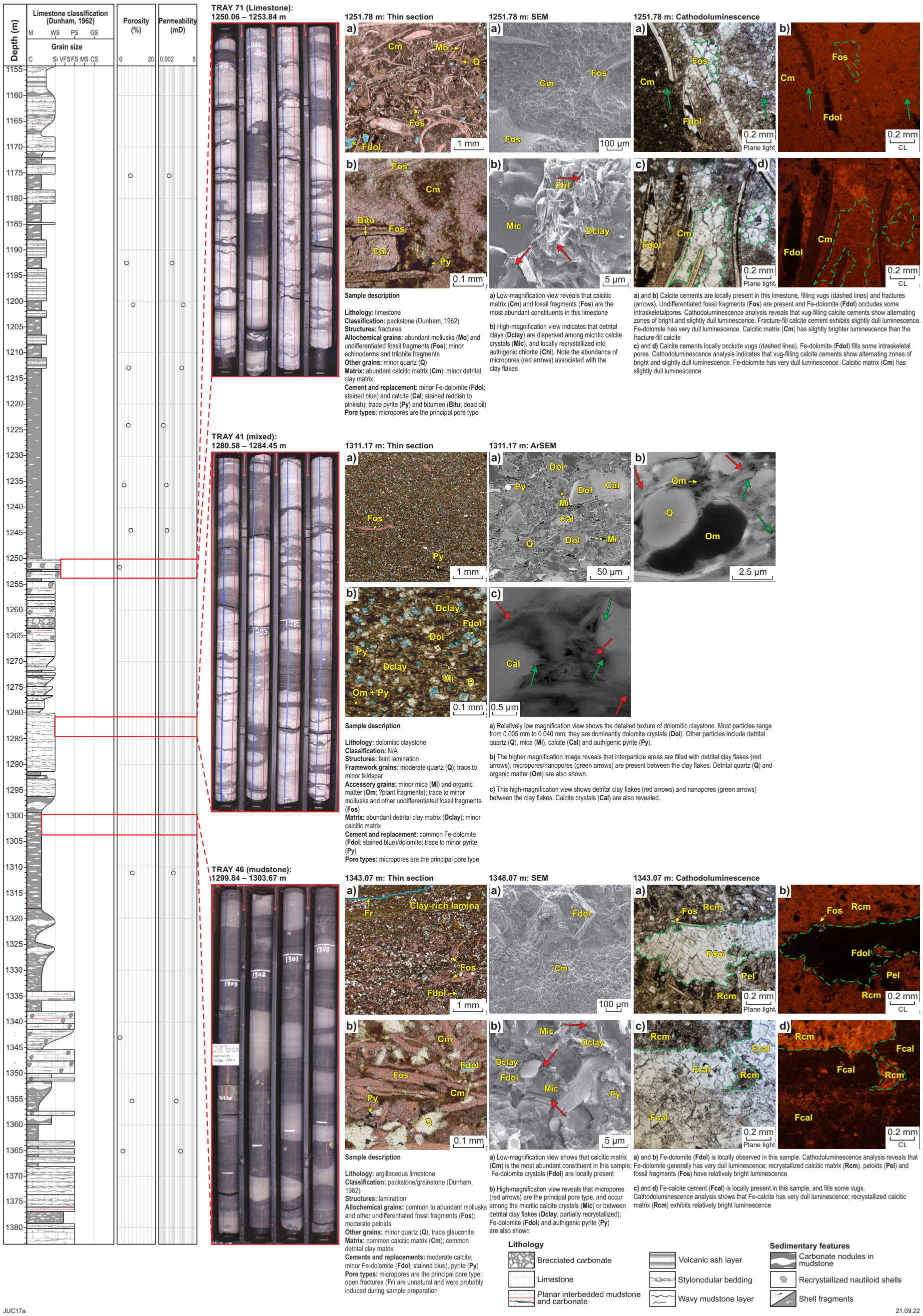

Figure 5.1. Core description with core-measured porosity and permeability and a selection of core photos and petrographic studies describing typical lithologies in the Samphire Marsh Member

RECORD 2022/13

PETROPHYSICAL EVALUATION OF THE PERMIAN AND ORDOVICIAN IN OLYMPIC 1, CANNING BASIN, WESTERN AUSTRALIA

J Cass, L Normore, L Dent and J Roche

Access GSWA products

All products
All GSWA products are free to download as PDFs from the DMIRS eBookshop <www.dmirs.wa.gov.au/ebookshop>.
View other geoscience information on our website <www.dmirs.wa.gov.au/gswa>.

Hard copies
Limited products are available to purchase as hard copies from the First Floor Counter at Mineral House or via the DMIRS eBookshop <www.dmirs.wa.gov.au/ebookshop>.

Fieldnotes
Fieldnotes is a free digital-only quarterly newsletter which provides regular updates to the State's exploration industry and geoscientists about GSWA's latest programs, products and services.
Access by subscribing to the GSWA eNewsletter <www.dmirs.wa.gov.au/gswaenewsletter> or downloading the free PDF from the DMIRS eBookshop <www.dmirs.wa.gov.au/ebookshop>.

GSWA eNewsletter
The GSWA eNewsletter is an online newsletter that contains information on workshops, field trips, training and other events.
To keep informed, please subscribe <www.dmirs.wa.gov.au/gswaenewsletter>.

Further details of geoscience products are available from:

First Floor Counter
Department of Mines, Industry Regulation and Safety
100 Plain Street
EAST PERTH WESTERN AUSTRALIA 6004
Phone: +61 8 9222 3459 Email: publications@dmirs.wa.gov.au
www.dmirs.wa.gov.au/GSWApublications